

# Resonant standing internal waves in a basin filled with two liquids separated by a pycnocline

Sabrina Kalenko<sup>1,2</sup> , E. Mogilevskiy<sup>1</sup> , E. Zemach<sup>2,3</sup> and L. Shemer<sup>1</sup> 

<sup>1</sup>School of Mechanical Engineering, Tel Aviv University, Tel Aviv, Israel

<sup>2</sup>Soreq Nuclear Research Center (SNRC), Yavne, Israel

<sup>3</sup>Sami Shamoon College of Engineering, Beer Sheva, Israel

**Correspondence author:** L. Shemer, [shemerl@tauex.tau.ac.il](mailto:shemerl@tauex.tau.ac.il)

(Received 14 October 2024; revised 2 April 2025; accepted 7 April 2025)

Combined theoretical and quantitative experimental study of resonant internal standing waves in a pycnocline between two miscible liquids in a narrow rectangular basin is presented. The waves are excited by a cylinder that harmonically oscillates in the vertical direction. A linear theoretical model describing the internal wave structure that accounts for pycnocline thickness, the finite wavemaker size and dissipation is developed. Separate series of measurements were performed using shadowgraphy and time-resolved particle image velocimetry. Accurate density profile measurements were carried out to monitor the variation of the pycnocline parameters in the course of the experiments; these measurements were used as the input parameters for the model simulations. The detected broadening of the pycnocline is attributed mainly to the presence of the waves and leads to the variation of the wave structure. The complex spatio-temporal structure of the observed internal wavefield was elucidated by carrying band-pass filtering in the temporal domain. The experiments demonstrate the coexistence of multiple spatial modes at the forcing frequency as well as the presence of the internal wave system at the second harmonic of the forcing frequency. The results of the theoretical model are in good agreement with the experiments.

**Key words:** internal waves, stratified flows, general fluid mechanics

## 1. Introduction

Internal gravity waves observed in stably stratified fluids play an essential role in the transport of momentum, energy and mass in oceans, lakes and atmosphere. Therefore,

different aspects related to the internal wave dynamics continue to be a subject of active research (e.g. Mathur & Peacock 2010; Hussein *et al.* 2020; Rodda *et al.* 2022; Lanchon & Cortet 2023; Yalim *et al.* 2023). The structure of internal waves depends significantly on the stratification profile; waves at the interface separating two sufficiently thick layers of immiscible homogeneous liquids with different densities represent an important limiting case (Lamb 1932). The waves at a free water surface can be seen as a particular case of such a two-layer system when the density of the lighter fluid can be neglected.

The dispersion relation between the angular frequency  $\omega$  and the horizontal wavevector  $\mathbf{k}$  for waves at a horizontally unlimited interface between two liquids with densities  $\rho_1 < \rho_2$  is

$$\omega^2 = g'|\mathbf{k}|, \quad g' = g \frac{\rho_2 - \rho_1}{\rho_2 + \rho_1}, \quad (1.1)$$

where  $g$  is the acceleration due to gravity. In the case of miscible liquids, a pycnocline separating the layers of constant density is formed where the density varies with the vertical coordinate  $z$ , defining the local non-zero buoyancy frequency  $N$  (Lighthill 1978):

$$N^2(z) = -\frac{g}{\rho(z)} \frac{d\rho(z)}{dz}. \quad (1.2)$$

In this configuration more complex wave systems are possible. Time-dependent disturbances introduced in the bulk of one of the liquids may produce a superposition of symmetric and antisymmetric wavemodes propagating along the pycnocline (Davis & Acrivos 1967*b*). Antisymmetric solitary waves (sometimes referred to as mode-2 internal solitary waves) are observed in laboratory experiments (Davis & Acrivos 1967*a*; Cheng & Hsu 2014; Deepwell & Stastna 2016), as well as in nature (Farmer & Smith 1980; Yang *et al.* 2009; Shanmugam 2013). The dispersion relation between the set of possible  $\omega$  for any given  $\mathbf{k}$  is defined by a solution of the Sturm–Liouville problem (Benjamin 1967; Miles 1971) and was approximated by Barber (1993).

In experiments on both surface and internal waves carried out in a closed laboratory facility, spatial confinement by vertical walls imposes limitations on possible wavevectors due to non-penetration boundary conditions (Thorpe 1968; Faltinsen 1974; Geva *et al.* 2021); in a deep narrow basin of length  $L$  and width  $B \ll L$ , these wavevectors are  $\mathbf{k} = (k_n, 0)$ ,  $k_n = \pi n/L$ . The frequency of waves excited by externally controlled periodic motion of a rigid body is set by the forcing. In such experiments, a mismatch can exist between the forcing frequency  $\omega$  and eigenfrequencies prescribed by the reservoir geometry wavenumbers  $k_n$  via the dispersion relation (1.1). Additional adjustment of the eigenfrequencies is caused by the presence of the rigid wavemaker body within the liquid. The corresponding problem for a wavemaker-excited resonant standing surface gravity wave system in a narrow reservoir that accounts for the contribution of both the sidewalls and the wavemaker was solved by Mogilevskiy *et al.* (2024). They demonstrated theoretically the existence of multiple spatial modes in the resonant wave spectrum, and validated those results in experiments.

The internal wavefield excited by a wavemaker in a deep narrow cavity filled by two liquids separated by a finite-thickness pycnocline is even more complicated. In this case, not only do multiple modes with different wavevectors coexist, but also for any given resonant wavenumber  $k_n$ , modes with different vertical structures are possible. The internal structure within the pycnocline could not be captured in the study of wavemaker-excited resonant standing waves by Thorpe (1968) that was based on shadowgraph imaging. Since then, various optical methods have been applied to the study of internal waves, such as time-resolved particle image velocimetry (PIV)

(Mathur & Peacock 2010; Dossmann *et al.* 2011; Carr *et al.* 2015; Boury *et al.* 2019), planar laser-induced fluorescence (Troy & Koseff 2005; Dossmann *et al.* 2016) and synthetic schlieren (Sutherland *et al.* 1999; Dalziel *et al.* 2000).

Modern video-based optical methods are applied here to study wavemaker-excited resonant standing waves in a narrow long basin within a pycnocline between two layers of liquids that slightly differ in density. This allows one to expand significantly the analysis of the system studied by Thorpe (1968) to reveal the effect of the pycnocline thickness on the complicated spatio-temporal structure of the internal wavefield within it. The experimental facility is described in § 2; in § 3, the analysis of the shadowgraph video recording is coupled with density profile measurements. These preliminary experiments prompted the development of a theoretical model based on the approach by Mogilevskiy *et al.* (2024) in § 4. The theoretical prediction of the coexistence of symmetric and antisymmetric modes in the internal resonant standing wave within the pycnocline is verified quantitatively by PIV-derived data in § 5. Section 6 summarises the study.

## 2. Experimental set-up and shadowgraph procedure

Experiments were carried out in an  $L = 772$  mm long and  $B = 160$  mm wide basin filled by layers of salted and pure water separated by a thin pycnocline. Stable stratification is attained by filling the basin first to a depth of 400 mm with  $\text{MgCl}_2$  solution. Pure water is then gently added through a sponge that floats on the surface, until the total depth of the liquid in the basin reaches 700 mm. The densities of pure water ( $\rho_1 = 998.5 \text{ kg m}^{-3}$ ) and of the salt solution ( $\rho_2 = 1020 \text{ kg m}^{-3}$ ) are measured using a Mettler Toledo densitometer. Inevitable mixing results in the formation of a finite-thickness pycnocline in which the density varies between its extreme values; the initial characteristic pycnocline thickness is about 14 mm. The density profile was determined with a high-precision conductivity probe (PCP) connected to a computer-controlled stage with a vertical resolution of 1 mm. The gradual increase of the actual thickness of the pycnocline in the course of experiments was monitored between the experimental runs by the PCP. A schematic sketch of the experimental set-up is presented in figure 1.

Waves were excited by a cylinder  $2R = 42$  mm in diameter; its axis is horizontal and spans the whole width of the basin. The wavemaker is supported by a thin rod connected to a linear computer-controlled motor that generates vertical harmonic oscillations. The mean position of the wavemaker centre is 350 mm above the bottom of the basin in the heavier layer. The instantaneous vertical position was recorded using a laser position sensor and served as a phase reference.

The two-layer model predicts the standing-wave frequency for the  $n$ th spatial mode as

$$\omega_n^2 = \left( \frac{2\pi}{T_n} \right)^2 = \frac{g(\rho_2 - \rho_1)}{\rho_2 + \rho_1} k_n, \quad k_n = \frac{n\pi}{L}. \quad (2.1)$$

Mostly, the experiments were performed for  $n = 3$  and some of them for  $n = 4$  corresponding to oscillation periods of  $T_3 = 5.56$  s and  $T_4 = 4.85$  s, and wavelengths  $\lambda_3 = 514$  mm and  $\lambda_4 = 386$  mm. For both modes, the effects of the bottom and of the free surface of the lighter liquid are negligible as the thicknesses of both layers are sufficiently large ( $D_{1,2} > 300$  mm); the resulting correction to the dispersion relation (2.1) does not exceed 0.2 %. The centre of the wavemaker was positioned at the antinode of the corresponding resonant mode, at a distance  $L/3$  from the sidewall for the experiments at  $n = 3$  and  $L/2$  for those at  $n = 4$ .

Preliminary experiments were carried out to determine the frequency range of maximum response. After that, a detailed frequency scan was performed. Those preliminary

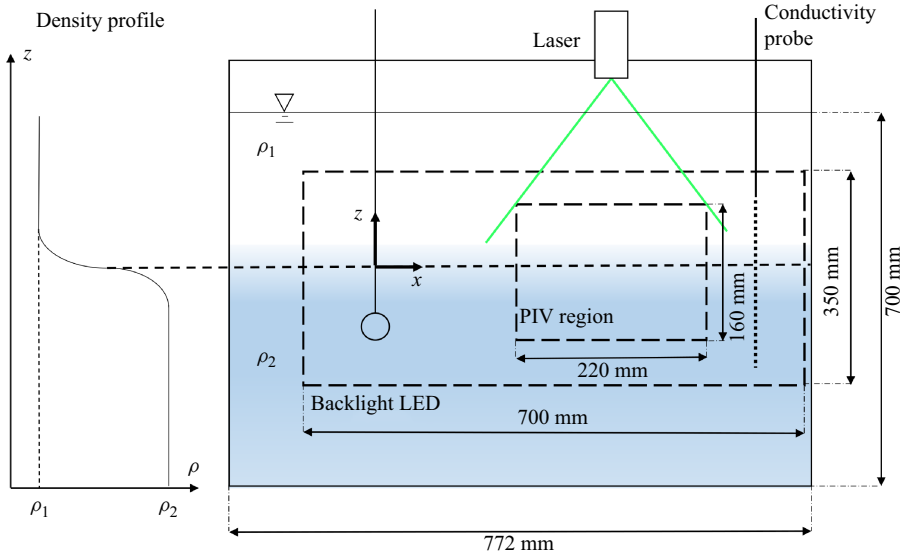


Figure 1. Sketch of the experimental system (front view); the basin is 160 mm wide. The origin of axes:  $x = 0$  at the wavemaker location;  $z = 0$  at the maximum of the density gradient at rest.

experiments clearly indicated that significant amplitudes of the internal waves are observed for frequencies below  $\omega_n$  in the typical range of the normalised frequency:

$$0.88 < \alpha = \frac{\omega}{\omega_n} < 0.97. \quad (2.2)$$

Each experimental run for prescribed wavemaker amplitude  $F$  and normalised frequency  $\alpha$  starts with the liquid at rest. The wavemaker operation lasts for about 30 min (300 periods). The wavemaker then stops and the recording continues until the waves practically vanish due to dissipation. The run finished with the measurement of the density profile by the PCP. The whole experiment is fully automated with LabView software that controls and synchronises the operation of all elements and data recording.

Figure 2 describes the evolution of the density distribution during a series of 12 experimental runs for  $n = 3$  with 12 equally spaced frequencies ranging from  $\alpha_{min} = 0.89$  to  $\alpha_{max} = 0.94$ ;  $F = 7.5$  mm. Density profiles measured prior to the first run and following the last run are plotted in figure 2(a). During the course of the experiment, the thickness of the pycnocline grows; it is defined as

$$d = \frac{(\rho_2 - \rho_1)}{|d\rho/dz|_{max}}, \quad (2.3)$$

where  $|d\rho/dz|_{max}$  is the density gradient maximum (figure 2b). Note that the measurements of the density profile performed repeatedly each 30 min in a constantly stagnant liquid with the wavemaker at rest during 12 hours demonstrated negligible change in  $d$  due to molecular diffusion. Indeed, for a diffusion coefficient  $\kappa \sim 10^{-3} \text{ mm}^2 \text{ s}^{-1}$ , the estimate of the widening of the pycnocline with time  $t$  as  $d^2(t) - d^2(t_0) \sim \kappa(t - t_0)$  yields the growth of the pycnocline thickness  $d$  that is below 10 %.

The density gradient distribution characterised by the buoyancy frequency (1.2) becomes wider with a corresponding decrease of the maximum  $N_{max}^2$  (figure 2c). However,

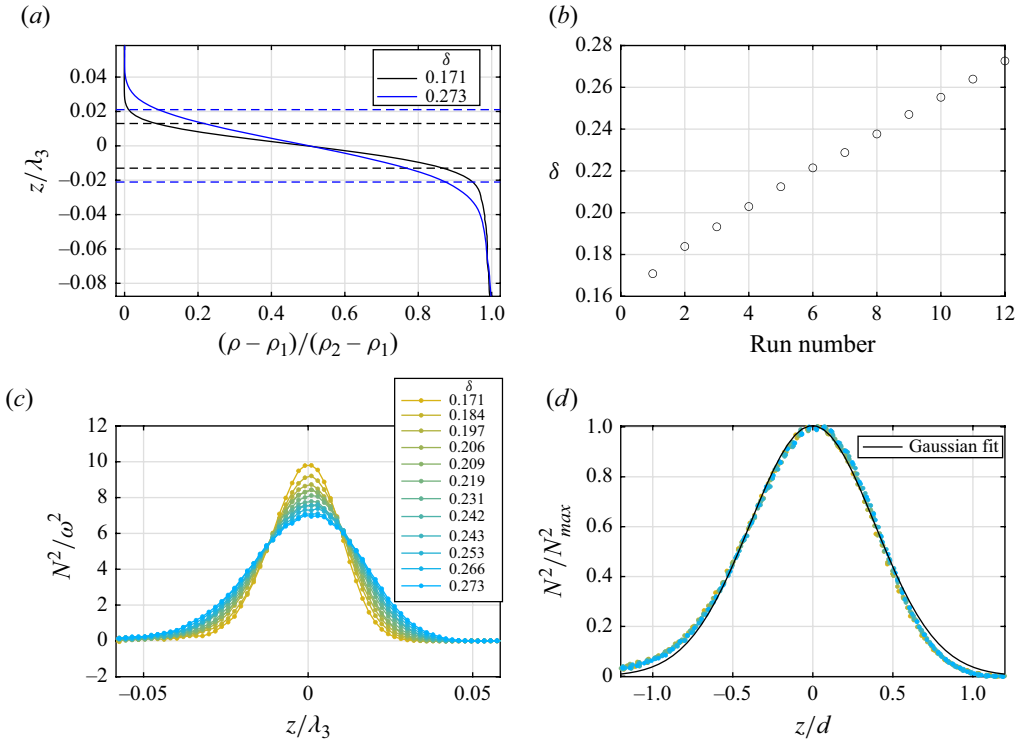


Figure 2. Density profile evolution during experiments at  $F = 7.5$  mm, and  $0.89 \leq \alpha \leq 0.94$ . (a) The measured extreme density profiles. The dashed horizontal lines mark the effective pycnocline boundaries  $\pm d/(2\lambda_3)$ . (b) The variation of the dimensionless pycnocline thickness  $\delta$  as a function of run number. (c) Corresponding distributions of buoyancy frequency. (d) Collapse of the normalised distributions. This and subsequent figures correspond to  $n = 3$ , unless specified explicitly otherwise.

the shape of the normalised profiles  $N^2(z/d)/N_{max}^2$  does not change notably and is well approximated by a Gaussian (figure 2d):

$$N^2 = \frac{2g(\rho_2 - \rho_1)}{d(\rho_2 + \rho_1)} \exp\left(-\pi \frac{z^2}{d^2}\right) = 2 \frac{(\omega_n)^2}{k_n d} \exp\left(-\pi \frac{z^2}{d^2}\right). \quad (2.4)$$

The non-dimensional buoyancy frequency is defined as

$$\tilde{N}^2 = \frac{2}{\delta} \exp\left(-\pi \frac{z^2}{d^2}\right), \quad \delta = k_n d. \quad (2.5)$$

Experiments were first performed using the shadowgraph technique that gives wide spatial coverage; after that, the internal structure of the waves was extracted using PIV data.

### 3. Shadowgraph experiments

For shadowgraph experiments, a fluorescent dye added to the heavier fluid forms a distinct boundary in the images (figure 3). Two back-light square LED panels adjacent to the back wall of the basin provide uniform illumination over the total area of  $350 \text{ mm} \times 700 \text{ mm}$  which is captured by a camera (3.2 MPixel USB 3.1 Flir Blackfly) at 10 frames per second.

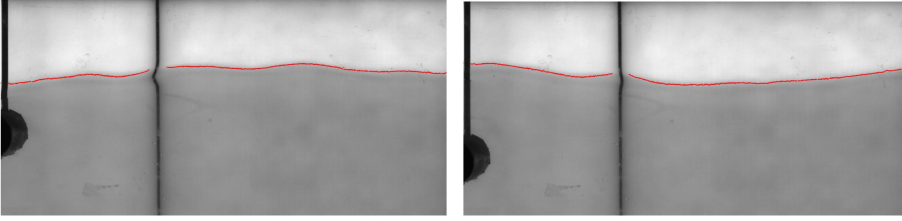


Figure 3. Two shadowgraph images shifted in time by half a wavemaker period. Supplementary movie 1 available at <https://doi.org/10.1017/jfm.2025.384> shows the movement of the detected interface.

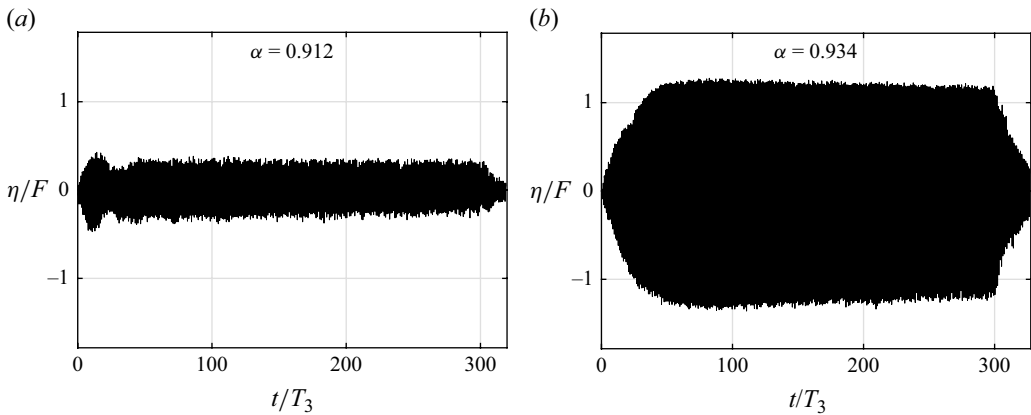


Figure 4. Dimensionless interface elevation  $\eta/F$  at antinode ( $x/\lambda_3 = 0.5$ ) of the third mode as a function of time, for wavemaker amplitude  $F = 5.6$  mm and (a,b) different forcing frequencies.

The location of the sharp interface clearly visible in figure 1 was extracted using an edge-detection procedure. The LED panel joint and the rod supporting the wavemaker cause two small gaps where the interface location cannot be determined.

The comparison of the processed images with the PCP data demonstrated that the interface location  $z = \zeta(t, x)$  in the images corresponds to the upper edge of the pycnocline. Figure 4 shows the normalised interface elevation

$$\eta(t, x) = \zeta(t, x) - \zeta(0, x) \quad (3.1)$$

at the antinode of the third mode ( $x/\lambda_3 = 0.5$ ) for the wavemaker amplitude  $F = 5.6$  mm as a function of time for two forcing frequencies;  $\alpha = 0.93$  (figure 4b) corresponds to the effective resonance. The initial transient stage lasts about 25–50 periods of wavemaker oscillations and is followed by a quasi-steady stage. The slow variation of the wave amplitude at this stage can be attributed to the growth of the mixing layer in the course of the run. The termination of the wavemaker operation results in a decay of waves at a time scale comparable with that of the initial transient stage.

### 3.1. Results of the measurements

The apparently sinusoidal temporal variation of the interface elevation above the wavemaker is plotted in figure 5 together with the records of the wavemaker motion at different forcing frequencies. An effective resonance is observed at  $\alpha$  about 0.93; at lower frequencies, the interface oscillations at this lateral location are approximately in antiphase relative to the wavemaker motion. The phase difference seems to decrease notably as the

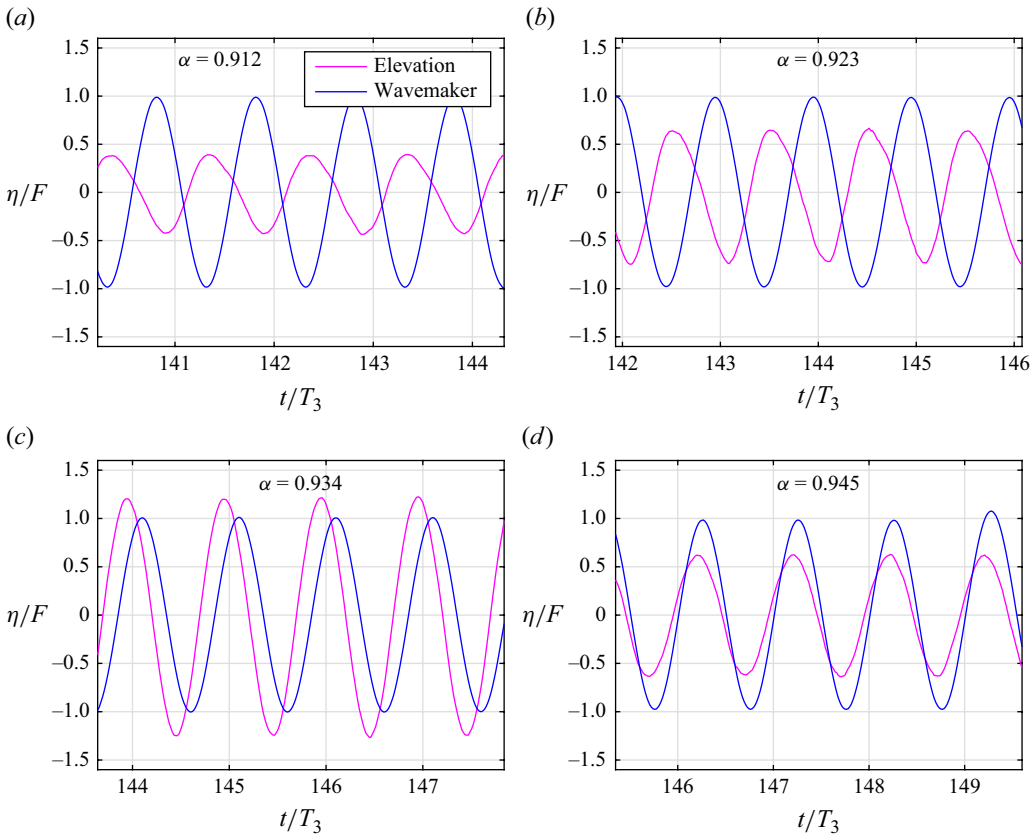


Figure 5. Short simultaneous records of interface elevation at the third-mode antinode  $x/\lambda_3 = 0.5$  and wavemaker movement for (a–d) different forcing frequencies; experimental conditions as in figure 4.

forcing frequency exceeds the effective resonance; in figure 5(d), the oscillations are nearly in phase.

Several instantaneous interface shapes are plotted in figure 6(a). While those shapes indeed seem to be dominated by the resonant standing wave with  $m = 3$ , they clearly contain contributions from additional shorter waves. The appearance of shorter waves is more pronounced for frequencies below the resonant frequency (dashed curves in figure 6a). The root-mean-square  $\langle \eta^2 \rangle^{1/2}$  values of the interface elevation were calculated separately for each horizontal location  $x$  (figure 6b) and averaged over 220 periods corresponding to the quasi-steady state. For a monochromatic standing wave, the expected values of  $\langle \eta^2 \rangle^{1/2}$  are zero at nodes spaced by half a wavelength, and reach their maximum at antinodes. Figure 6(b) demonstrates that this pattern describes the actual behaviour only approximately; the values of  $\langle \eta^2 \rangle^{1/2}$  do not vanish at nodes, and the shapes around the antinodes are quite flat. At frequencies well below the effective resonance, the measured distributions of  $\langle \eta^2 \rangle^{1/2}$  are nearly flat everywhere. The complexity of the interface wavy shape manifests itself in the wavenumber spectra of the complex amplitude of the interface shape band-pass-filtered at the forcing frequency (figure 7). Along with the global maxima at  $m = 3$ , the additional weaker local maxima at  $m \approx 9$  and  $m \approx 15$  are seen. The former can be attributed to the cubic nonlinearity and the interaction of the dominant wavemode with itself, while the latter has no analogy in the surface waves.

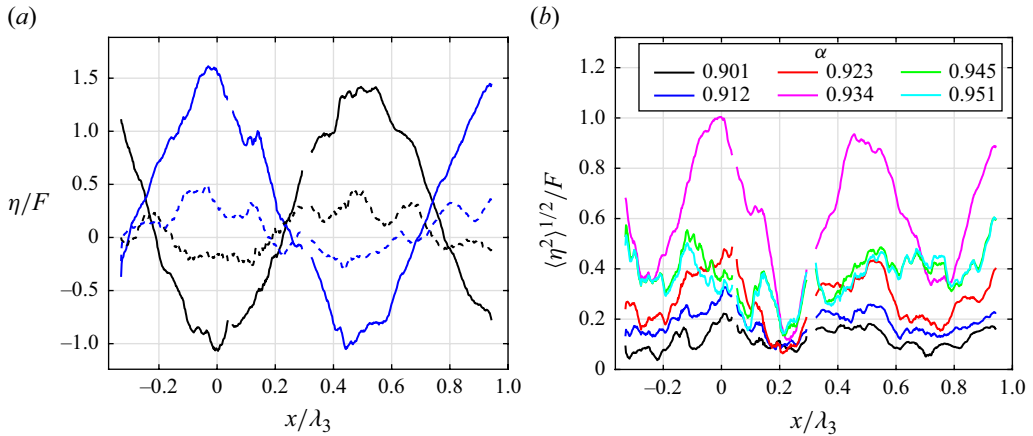


Figure 6. (a) Instantaneous interface shape for instants with maximum and minimum values of  $\eta$  at  $x=0$ . Dashed and solid lines are for the frequencies from figure 4(a) and 4(b), respectively. (b) Root-mean-square values of interface elevation at different forcing frequencies.

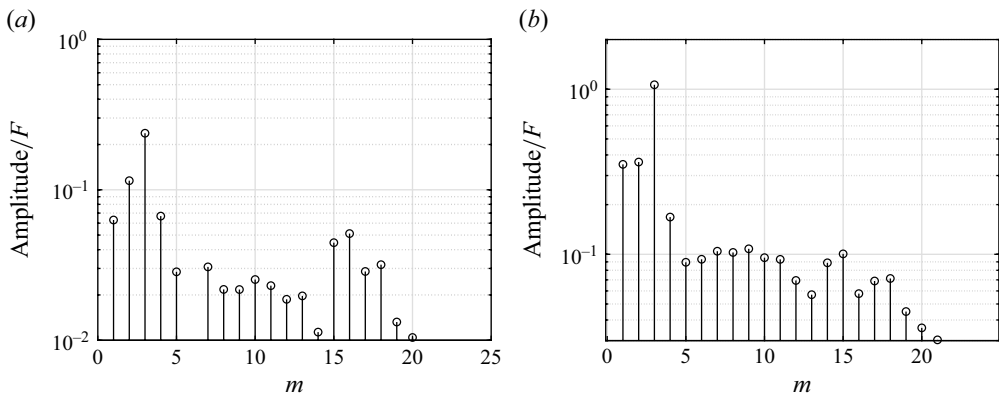


Figure 7. Wavenumber amplitude spectra of the temporal amplitudes of the interface shape band-pass-filtered at the forcing frequency, for (a,b) the cases shown in figure 4(a) and 4(b), respectively.

The frequency spectrum of the interface elevation at the antinode is dominated by a harmonic at the wavemaker driving frequency (figure 8a); this harmonic, while much weaker, is also notable at the node of the standing wave (figure 8b). At both the node and the antinode, there is a significant peak at double the wavemaker frequency, which is more pronounced when the forcing frequency is below the effective resonance (figure 8a).

The variation of the amplitude of the interface elevation with forcing frequency is plotted in figure 9(a) for three values of the wavemaker amplitude obtained in a single series of experimental runs with increasing forcing frequency. The effective resonance downshifts as the forcing amplitude increases. The pycnocline thickness  $d$  grows so that  $\delta$  changes from about 0.17 to about 0.25 as shown in figure 9 by colours of the markers. The decrease of the phase shift between the interface elevation above the wavemaker and the wavemaker from  $\pi$  towards zero is plotted for those runs in figure 9(b).

The effect of the pycnocline thickness widening in the course of the experiment is studied in an additional series of experiments carried out for  $n=4$ . Those runs started from the lowest frequency with  $\alpha=0.92$ , attained the value of forcing frequency

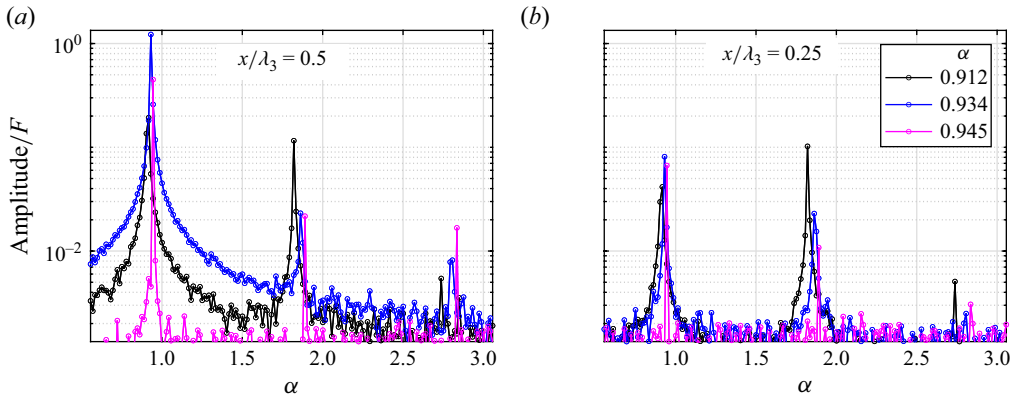


Figure 8. Normalised amplitude frequency spectra of interface elevation for wavemaker amplitude  $F = 5.6$  mm: (a) at the antinode ( $x/\lambda_3 = 0.5$ ); (b) at the node ( $x/\lambda_3 = 0.25$ ).

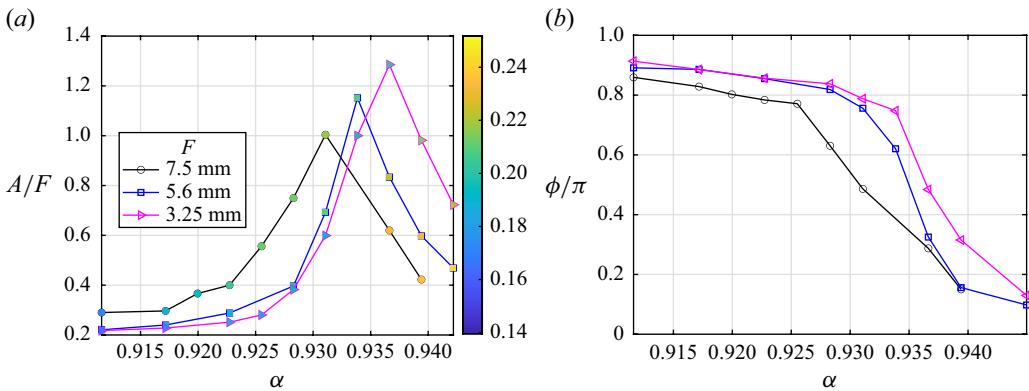


Figure 9. (a) Interface elevation amplitude in the antinode ( $x/\lambda_3 = 0.5$ ) for different forcing amplitudes, the coloured symbols represent the pycnocline thickness  $\delta$ . (b) Phase difference between the surface elevation and the wavemaker displacement for the cases as in (a).

$\alpha = 0.978$ , after which the values of  $\alpha$  were gradually decreased. Figure 10 shows the downshift of the resonant frequency with an increase of  $\delta$ .

### 3.2. Interim conclusions

Shadowgraph experiments reveal the basic features of internal waves in a closed basin containing two liquids with different densities separated by a relatively thin pycnocline. The complex structure of the wave, excited by a wavemaker operating in the vicinity of the resonant frequency corresponding to the selected two-layer mode, is exposed in the temporal records of the visible interface elevation. The temporal spectra at any longitudinal location are dominated by discrete harmonics corresponding to the wavemaker forcing frequency  $\omega$  and its second harmonic  $2\omega$ . The resonant wave in the vicinity of the third-mode resonant frequency clearly deviates from the sinusoidal shape: the wavenumber spectra of records band-pass-filtered at the forcing frequency (figure 7) contain multiple components with  $m$  in the vicinity of the resonant mode  $n = 3$ , components with  $m \approx 3n$  that may be attributed to cubic nonlinearity and  $m \approx 15$  that, as will be shown in the following, are related to the finite pycnocline thickness. The effective resonance frequency

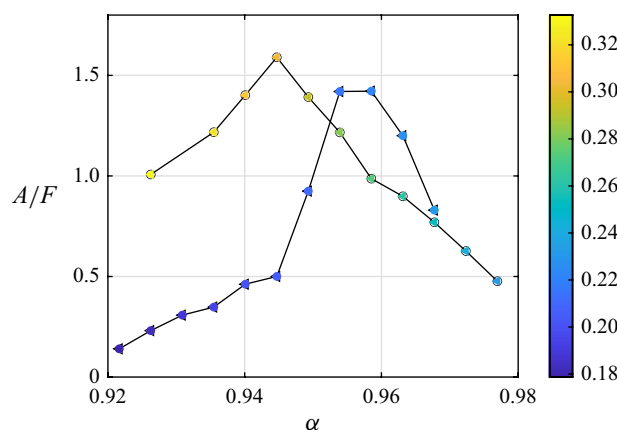


Figure 10. Interface elevation amplitude at the antinode ( $n = 4$ ,  $x/\lambda_4 = 0.25$ ,  $F = 10$  mm). The coloured symbols represent the pycnocline thickness  $\delta$ .

in the experiments is apparently downshifted from the two-layer model prediction  $\omega_n$ ; this downshift increases with an increase of the wavemaker amplitude  $F$ .

The thickness of the pycnocline  $d$  increases in the course experimental sessions. The increase in  $d$  affects notably the effective resonance of the system; it also contributes to the downshift of the effective resonant frequency. It should be emphasised that while the density distribution can be monitored between the runs using the PCP, there is no way to control it.

The shadowgraph experiments have the advantage of wide spatial coverage, but the sequence of recorded images only provides information on the movement of one surface representing the effective interface. This technique is thus incapable of revealing the full internal wave structure inside a pycnocline of finite thickness, suggesting that a different experimental approach is needed. The PIV technique can provide the necessary two-dimensional information; however, carrying out these experiments for a wide range of parameters requires extensive resources. An efficient experimental programme can benefit from guidelines supplied by a theoretical model that gives prior estimates of the wavefield behaviour.

#### 4. Theoretical model

Modelling of surface water waves is routinely based on the assumption of irrotational flow within the liquid governed by the Laplace equation; due to the Green theorem once the free-surface boundary conditions are satisfied, the flow in the bulk can be computed (see e.g. Newman 2018). For stratified media, neglecting the thickness of the pycnocline results in the two-layer model with the dispersion relation (1.1) for linear waves (Lamb 1932). Methods developed for accounting for nonlinear effects associated with the finite wave amplitude (e.g. Penny 1952) applied to a two-layer model by Thorpe (1968) showed the appearance of a bound wave with double wavenumber and frequency and a decrease of the wave celerity associated with the wave steepness. The generalisation of this approach to account for continuous stratification by Miles (1986) resulted in a variational formulation capable of describing weakly nonlinear propagating waves in arbitrary stably stratified pycnoclines. The similarity between the surface and the internal waves within the two-layer model enables estimates of the effect of the internal wave amplitude using the results

obtained for resonantly forced surface waves (Moiseev 1958; Faltinsen 1974; Mogilevskiy *et al.* 2024).

The internal wavefield structure is affected by the finite pycnocline thickness at any wave amplitude. As shown by Miles (1971), the flow within the pycnocline is not potential; thus, the dispersion relation cannot be obtained explicitly. It can be obtained by solving the Sturm–Liouville problem for a given density distribution. Besides, continuous stratification does not allow introduction of a distinct horizontal boundary where boundary conditions can be stated as in the two-layer model.

In this section, the resonant surface wave model (Mogilevskiy *et al.* 2024) is first adjusted to a two-layer system. Then, an analytical solution is presented for continuous stratification approximated by a piecewise-constant profile of the buoyancy frequency  $N^2(z)$ , while neglecting the wavemaker size. Finally, a numerical method that accounts for viscous dissipation, arbitrary stratification and the wavemaker geometry is introduced.

#### 4.1. Two-layer model

Consider two-dimensional flow in the  $(x, z)$  plane of two effectively infinite deep layers of homogeneous liquids separated by interface  $z = \eta(x, t)$ . The variables are rendered dimensionless as

$$(\tilde{x}, \tilde{z}) = k_n(x, z), \quad \tilde{t} = \omega t. \quad (4.1)$$

The velocity is scaled by  $\omega F$ ; the interface location by  $F$ :

$$\tilde{\eta} = \frac{\eta}{F}. \quad (4.2)$$

The dimensionless wall locations are  $\tilde{x} = -\pi$  and  $\tilde{x} = (n-1)\pi$ . The mean position of the interface is  $\tilde{\eta} = 0$ . The dimensionless parameters  $r$  and  $h$ ,

$$r = k_n R, \quad h = k_n H, \quad (4.3)$$

define the geometry of the wavemaker;  $-H$  is the mean vertical coordinate of its centre. For  $n = 3$ , the experiments correspond to  $r = 0.26$ ,  $h = 0.71$ . The instantaneous location of the wavemaker centres

$$\tilde{z}_c(\tilde{t}) = -h + \varepsilon \sin \tilde{t}, \quad \varepsilon = k_n F. \quad (4.4)$$

The flow is assumed irrotational in both layers; the dimensionless velocity potentials  $\varphi_1$  and  $\varphi_2$  in the upper and lower liquids satisfy the Laplace equation:

$$\nabla^2 \varphi_1 = 0, \quad -\pi < \tilde{x} < (n-1)\pi, \quad \tilde{z} > \tilde{\eta}(\tilde{x}, \tilde{t}), \quad (4.5a)$$

$$\nabla^2 \varphi_2 = 0, \quad -\pi < \tilde{x} < (n-1)\pi, \quad \tilde{z} < \tilde{\eta}(\tilde{x}, \tilde{t}), \quad \tilde{x}^2 + (\tilde{z} - \tilde{z}_c(\tilde{t}))^2 > r^2. \quad (4.5b)$$

The non-penetration conditions at the rigid boundaries (walls and the wavemaker) are

$$\frac{\partial \varphi_1}{\partial \tilde{x}} = 0, \quad \tilde{x} = -\pi, (n-1)\pi, \quad (4.6a)$$

$$|\nabla \varphi_1| \rightarrow 0, \quad \tilde{z} \rightarrow \infty, \quad (4.6b)$$

$$\frac{\partial \varphi_2}{\partial \tilde{x}} = 0, \quad \tilde{x} = -\pi, (n-1)\pi, \quad (4.6c)$$

$$\frac{\partial \varphi_2}{\partial n} = \frac{1}{\varepsilon} \frac{d\tilde{z}_c}{d\tilde{t}} \frac{\tilde{z} - \tilde{z}_c}{r^2}, \quad \tilde{x}^2 + (\tilde{z} - \tilde{z}_c(\tilde{t}))^2 = r^2, \quad (4.6d)$$

$$|\nabla \varphi_2| \rightarrow 0, \quad \tilde{z} \rightarrow -\infty. \quad (4.6e)$$

The continuity of the vertical velocity and of the pressure at the interface connects the interface location  $\tilde{\eta}$  with the potentials:

$$\begin{aligned} \frac{\partial \varphi_1}{\partial \tilde{z}} &= \frac{\partial \varphi_2}{\partial \tilde{z}} \\ \tilde{z} = \tilde{\eta}(\tilde{x}, \tilde{t}) : \quad \frac{\partial \varphi_1}{\partial \tilde{t}} + \frac{\varepsilon}{2} (\nabla \varphi_1)^2 &= \frac{\rho_2}{\rho_1} \left[ \frac{\partial \varphi_2}{\partial \tilde{t}} + \frac{\varepsilon}{2} (\nabla \varphi_2)^2 \right] + \frac{(\rho_2 - \rho_1) g k_n}{\rho_1 \omega^2} \tilde{\eta} \\ \frac{\partial \tilde{\eta}}{\partial \tilde{t}} + \frac{\partial \varphi_1}{\partial \tilde{x}} \frac{\partial \tilde{\eta}}{\partial \tilde{x}} &= \frac{\partial \varphi_1}{\partial \tilde{z}}. \end{aligned} \quad (4.7)$$

Neglecting terms of the order of  $(\rho_2 - \rho_1)/\rho_1$  and  $\varepsilon$  and eliminating  $\eta$  yields a simplified linear problem for potentials:

$$\nabla^2 \varphi_1 = 0, \quad -\pi < \tilde{x} < (n-1)\pi, \quad \tilde{z} > 0, \quad (4.8a)$$

$$\nabla^2 \varphi_2 = 0, \quad -\pi < \tilde{x} < (n-1)\pi, \quad \tilde{z} < 0, \quad \tilde{x}^2 + (\tilde{z} + h)^2 > r^2, \quad (4.8b)$$

$$\frac{\partial \varphi_1}{\partial \tilde{x}} = 0, \quad \tilde{x} = -\pi, (n-1)\pi, \quad (4.8c)$$

$$|\nabla \varphi_1| \rightarrow 0, \quad \tilde{z} \rightarrow \infty, \quad (4.8d)$$

$$\frac{\partial \varphi_2}{\partial \tilde{x}} = 0, \quad \tilde{x} = -\pi, (m-1)\pi, \quad (4.8e)$$

$$\frac{\partial \varphi_2}{\partial n} = \frac{\tilde{z} + h}{r^2} \cos t, \quad \tilde{x}^2 + (\tilde{z} + h)^2 = r^2, \quad (4.8f)$$

$$|\nabla \varphi_2| \rightarrow 0, \quad \tilde{z} \rightarrow -\infty, \quad (4.8g)$$

$$\frac{\partial \varphi_1}{\partial \tilde{z}} = \frac{\partial \varphi_2}{\partial \tilde{z}}, \quad \tilde{z} = 0, \quad (4.8h)$$

$$\frac{\partial^2 \varphi_1}{\partial \tilde{t}^2} = \frac{\partial^2 \varphi_2}{\partial \tilde{t}^2} + \frac{2}{\alpha^2} \frac{\partial \varphi_2}{\partial \tilde{z}}, \quad \tilde{z} = 0. \quad (4.8i)$$

The violation of the symmetry between the upper and the lower liquids is due to the presence of the wavemaker under the interface. It leads to the failure of the solution of Lamb (1932) as it does not satisfy the boundary condition at the wavemaker (4.8f). The Lamb solution in the upper liquid is retained:

$$\varphi_1 = \sum_{m=1}^{\infty} a_m \varphi_{1,m}, \quad \varphi_{1,m} = \frac{1}{2} \left[ \cos \left( \frac{m}{n} (\tilde{x} + \pi) \right) \exp \left( -\frac{m}{n} \tilde{z} \right) \exp(-i\tilde{t}) + \text{c.c.} \right]. \quad (4.9)$$

In the lower liquid, the solution is represented as a superposition of the forcing potential  $\varphi_0$  and wavemodes  $\varphi_{2,m}$ :

$$\varphi_2 = \varphi_0 + \sum_{m=1}^{\infty} b_m \varphi_{2,m}. \quad (4.10)$$

The potential  $\varphi_0$  satisfies equation (4.8b) with boundary conditions (4.8e–g), including the inhomogeneous boundary condition (4.8f). The potentials  $\varphi_{2,m}$  satisfy the homogeneous boundary condition at the wavemaker:

$$\begin{aligned} \frac{\partial \varphi_{2,m}}{\partial n} &= 0, \quad \tilde{x}^2 + (\tilde{z} + h)^2 = r^2 \\ \varphi_{2,m} &= \frac{1}{2} \left\{ \left[ \cos \left( \frac{m}{n} (\tilde{x} + \pi) \right) \exp \left( \frac{m}{n} \tilde{z} \right) + \varphi'_{2,m} \right] \exp(-i\tilde{t}) + \text{c.c.} \right\}. \end{aligned} \quad (4.11)$$

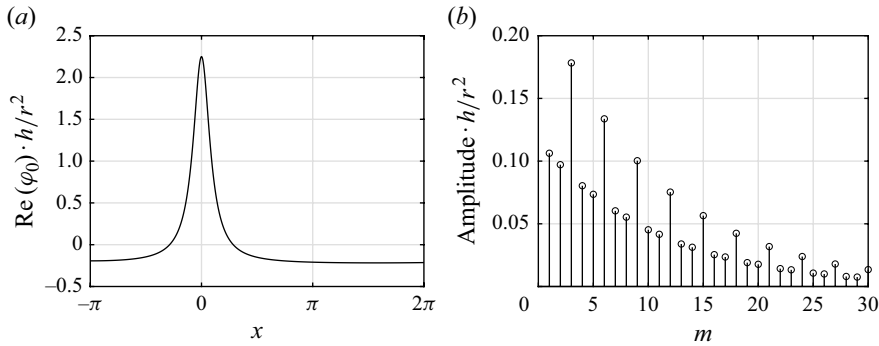


Figure 11. (a) Normalised forcing potential at  $\tilde{z} = 0$  and (b) its wavenumber amplitude spectrum.

The symmetry of the functions  $\varphi_0$  and  $\varphi'_{2,m}$  with respect to  $\tilde{z} = -h$  is also required for uniqueness; they are represented by series of multipoles placed at the wavemaker centre and their successive mirror reflections with respect to the basin walls (Mogilevskiy *et al.* 2024). The leading terms are

$$\begin{aligned}\varphi_0 &= \frac{1}{2} \left[ -\frac{r^2(z+h)}{x^2 + (z+h)^2} \exp(-i\tilde{t}) + \text{c.c.} \right]; \\ \varphi'_{2,m} &= \frac{1}{2} \left[ -\frac{m}{n} \exp\left(-\frac{m}{n}h\right) \frac{r^2(z+h)}{x^2 + (z+h)^2} \right].\end{aligned}\quad (4.12)$$

The forcing potential  $\varphi_0$  introduces disturbances of the order of  $r^2/h$  to all spatial modes (figure 11); the wavenumber spectrum has peaks at  $m = n, 2n, \dots$ , since the wavemaker is located at the antinode of those modes. The response of the system is defined by the boundary conditions (4.8h) and (4.8i) representing the continuity of the vertical velocity and the pressure at the interface. The substitution of (4.9), (4.10) yields the system of linear algebraic equations for  $a_m$  and  $b_m$ :

$$\begin{aligned}& \int_{-\pi}^{(n-1)\pi} \left[ \sum_{m=1}^{\infty} a_m \frac{\partial \varphi_{1,m}(\tilde{x}, 0)}{\partial \tilde{z}} - \sum_{m=1}^{\infty} b_m \frac{\partial \varphi_{2,m}(\tilde{x}, 0)}{\partial \tilde{z}} - \frac{\partial \varphi_0(\tilde{x}, 0)}{\partial \tilde{z}} \right] \cos\left(\frac{l}{n}(\tilde{x} + \pi)\right) d\tilde{x} = 0, \\ & \int_{-\pi}^{(n-1)\pi} \left\{ \sum_{m=1}^{\infty} a_m \varphi_{1,m}(\tilde{x}, 0) - \sum_{m=1}^{\infty} b_m \left[ \varphi_{2,m}(\tilde{x}, 0) - \frac{2}{\alpha^2} \frac{\partial \varphi_{2,m}(\tilde{x}, 0)}{\partial \tilde{z}} \right] \right. \\ & \quad \left. - \left[ \varphi_0(\tilde{x}, 0) - \frac{2}{\alpha^2} \frac{\partial \varphi_0(\tilde{x}, 0)}{\partial \tilde{z}} \right] \right\} \cos\left(\frac{l}{n}(\tilde{x} + \pi)\right) d\tilde{x} = 0, \\ & \quad l = 1 \dots \infty.\end{aligned}\quad (4.13)$$

The free terms associated with  $\varphi_0$  are of the order of  $r^2/h$  (see (4.12)). It can be shown that the eigenvalue of the system (4.13) is  $\alpha = m/n - \Delta\alpha_m$ , where  $0 < \Delta\alpha_m \sim r^2/(\pi nh)$  corresponds to the downshift of the resonant frequency due to the finite wavemaker size. For other values of  $\alpha$ , (4.13) has a unique solution.

This simplified two-layer model demonstrates the general approach; however, the predicted downshift of the resonant frequency from  $\alpha = 1$  is about 1%, an order of magnitude smaller than that measured in experiments (§ 3). The experimental results

plotted in [figure 10](#) indicate the significant effect of the thickness of the pycnocline, which is neglected in the two-layer model.

#### 4.2. Eigenfunctions for continuous stratification

In the linear approximation, the complex amplitude function for the vertical velocity  $W_m(\tilde{z})$  for a wave with the wavemode number  $m$  satisfies the Taylor–Goldstein equation (Goldstein 1931; Taylor 1931) for a given dimensionless buoyancy frequency distribution  $\tilde{N}(\tilde{z})$ :

$$W_m'' + \left( \frac{2}{\alpha^2} \tilde{N}^2 - 1 \right) \frac{m^2}{n^2} W_m = 0 \quad (4.14)$$

and the boundary conditions

$$W_m \rightarrow 0, \quad \tilde{z} \rightarrow \pm\infty, \quad (4.15)$$

where primes denote derivatives with respect to  $\tilde{z}$ . The analysis of this Sturm–Liouville problem shows that for any given  $m$ , there is an infinite number of solutions  $W_m^j$  and corresponding  $\alpha_{m,j}$  that are orthogonal with the weight function  $\tilde{N}^2$  (Morse & Feshbach 1946):

$$\int_{-\infty}^{\infty} W_m^{j_1} W_m^{j_2} \tilde{N}^2 d\tilde{z} = 0, \quad j_1 \neq j_2. \quad (4.16)$$

For the piecewise-constant distribution  $\tilde{N}^2(\tilde{z})$ :

$$\tilde{N}^2 = \begin{cases} 0, & \tilde{z} < -\delta/2 \\ \frac{1}{\delta}, & |\tilde{z}| < \delta/2 \\ 0, & \tilde{z} > \delta/2 \end{cases} \quad (4.17)$$

the analytical solution for  $W_m^j$  is

$$W_m^j = \begin{cases} \exp\left(\frac{m}{n}\tilde{z}\right), & \tilde{z} < -\frac{\delta}{2} \\ \cos(\gamma_m^j \tilde{z}) \exp\left(-\frac{m}{n}\frac{\delta}{2}\right) / \cos\left(\gamma_m^j \frac{\delta}{2}\right), & |\tilde{z}| < \frac{\delta}{2} \\ \exp\left(-\frac{m}{n}\tilde{z}\right), & \tilde{z} > \frac{\delta}{2} \end{cases} \quad j \text{ odd},$$

$$W_m^j = \begin{cases} -\exp\left(\frac{m}{n}\tilde{z}\right), & \tilde{z} < -\frac{\delta}{2} \\ \sin(\gamma_m^j \tilde{z}) \exp\left(-\frac{m}{n}\frac{\delta}{2}\right) / \sin\left(\gamma_m^j \frac{\delta}{2}\right), & |\tilde{z}| < \frac{\delta}{2} \\ \exp\left(-\frac{m}{n}\tilde{z}\right), & \tilde{z} > \frac{\delta}{2} \end{cases} \quad j \text{ even}, \quad (4.18)$$

where

$$\left(\gamma_m^j\right)^2 = \left( \frac{2}{\left(\alpha_m^j\right)^2 \delta} - 1 \right) \frac{m^2}{n^2} \quad (4.19)$$

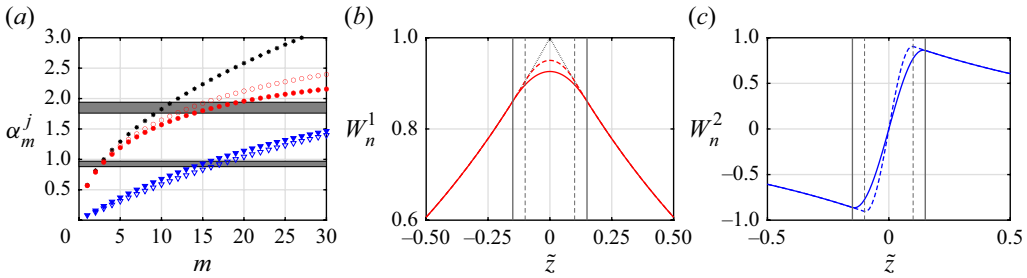


Figure 12. (a) Eigenfrequencies of the first symmetric ( $j = 1$ , red) and antisymmetric ( $j = 2$ , blue) modes for  $\delta = 0.2$  (open symbols) and  $\delta = 0.3$  (filled symbols); asterisks represent the two-layer model. The corresponding eigenfunctions  $W_n^1$  (b) and  $W_n^2$  (c) for  $\delta = 0.2$  (solid lines) and  $\delta = 0.3$  (dashed lines). The experimental ranges of the forcing frequency and its second harmonic are shaded in (a), the dotted line in (b) represents the eigenfunction for the two-layer model and the vertical lines in (b,c) show the boundaries of the pycnocline.

are roots of one of the equations:

$$\gamma \tan \frac{\gamma \delta}{2} = \frac{m}{n}, \quad (4.20a)$$

$$\gamma \cot \frac{\gamma \delta}{2} = -\frac{m}{n} \quad (4.20b)$$

(Miropol'sky & Shishkina 2001). Equations (4.20a) and (4.20b) correspond to the eigenvalues with odd and even superscript indices. The function  $W_m^j$  has  $j - 1$  zeros within the pycnocline; it is symmetric for odd  $j$  and antisymmetric for even  $j$  with respect to  $\tilde{z} = 0$ . The resonant mode in the two-layer model corresponds to  $\alpha_* = \alpha_n^1$ , in the limit  $\delta \ll 1$ ,

$$\alpha_* = 1 - \frac{\delta}{6} + O(\delta^2) \quad (4.21)$$

(Thorpe 1968). Figure 12 presents the eigenfrequencies  $\alpha_m^j$  as well as the eigenfunctions  $W_m^j$  for  $j = 1, 2$ . Note that  $W_m^j$  tends to the Lamb solution as  $\delta \rightarrow 0$ . For finite  $\delta$ , the eigenfrequency is downshifted from that of the Lamb solution by 6–10 % in the present experiments.

#### 4.3. Linear model for finite pycnocline thickness

The solution procedure follows the two-layer model approach. In this subsection, the simplified form of the potential solution (4.10) in the lower liquid ( $\tilde{z} < -\delta/2$ ) is used, neglecting terms  $\varphi'_{2,m}$  in (4.11) associated with the finite wavemaker size:

$$\varphi_2 = \varphi_0 + \frac{1}{2} \left[ \sum_{m=1}^{\infty} b_m \cos \left( \frac{m}{n} (\tilde{x} + \pi) \right) \exp \left( \frac{m}{n} \tilde{z} \right) \exp(-i\tilde{t}) + \text{c.c.} \right]. \quad (4.22)$$

The vertical velocity in the upper liquid, including the pycnocline, is the solution of the Taylor–Goldstein equation (4.14):

$$w = \frac{1}{2} \left[ \sum_{m=1}^{\infty} a_m W_m(\tilde{z}) \cos \left( \frac{m}{n} (\tilde{x} + \pi) \right) \exp(-i\tilde{t}) + \text{c.c.} \right]; \quad W_m \rightarrow 0, \quad \tilde{z} \rightarrow \infty. \quad (4.23)$$

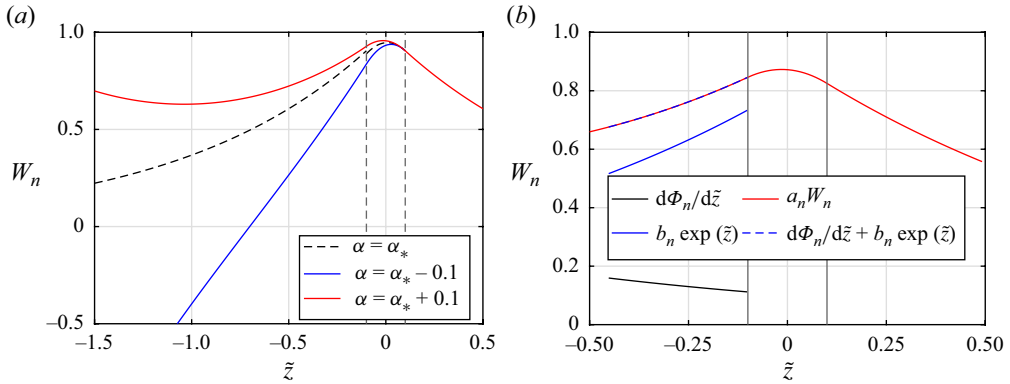


Figure 13. (a) The vertical velocity profiles  $W_n$  in the upper liquid extended to  $\tilde{z} < -\delta/2$ . (b) The sum of  $d\Phi_n/d\tilde{z}$  (in black) and  $b_n \exp(\tilde{z})$  (in blue) matches  $a_n W_n$  (in red); the coefficients are defined by (4.26). Thin vertical lines denote the boundaries of the pycnocline;  $\delta = 0.2$ ,  $\alpha = \alpha_* + 0.1$ .

Equation (4.14) is also valid in the lower liquid, so the solution can be smoothly extended to  $\tilde{z} < -\delta/2$ :

$$W_m = \begin{cases} C_1^m \exp\left(\frac{m}{n}\tilde{z}\right) + C_2^m \exp\left(-\frac{m}{n}\tilde{z}\right) & \tilde{z} < -\delta/2 \\ C_3^m \cos(\gamma\tilde{z}) + C_4^m \sin(\gamma\tilde{z}) & |\tilde{z}| < \delta/2 \\ \exp\left(-\frac{m}{n}\tilde{z}\right) & \tilde{z} > \delta/2 \end{cases} \quad \gamma^2 = \left(\frac{2}{\alpha^2\delta} - 1\right) \frac{m^2}{n^2}. \quad (4.24)$$

The constants  $C_1^m, \dots, C_4^m$  are found from the continuity conditions of  $W_m$  and  $W'_m$  at  $\tilde{z} = \pm\delta/2$ ; the coefficient at the exponent for  $\tilde{z} > \delta/2$  is chosen as unity for normalisation. For frequencies different from the eigenvalues  $\alpha \neq \alpha_m^j$ , the solution is unbounded as  $z \rightarrow -\infty$  ( $C_2^m \neq 0$ ). Examples of functions  $W_n$  are shown in figure 13(a).

Following Morse & Feshbach (1946), the contributions of the forcing potential  $\varphi_0$  to the  $m$ th spatial mode in the region between the wavemaker top and the lower boundary of the pycnocline  $-h + r < \tilde{z} < -\delta/2$  can be represented as

$$\Phi_m = \int_{-\pi}^{(n-1)\pi} \varphi_0(\tilde{x}, \tilde{z}) \cos\left(\frac{m}{n}(\tilde{x} + \pi)\right) d\tilde{x} = Q_1^m \exp\left(\frac{m}{n}\tilde{z}\right) + Q_2^m \exp\left(-\frac{m}{n}\tilde{z}\right). \quad (4.25)$$

The conditions

$$\begin{aligned} \frac{m}{n} Q_2^m &= \frac{1}{2} n\pi C_2^m a_m, \\ -\frac{m}{n} Q_1^m + \frac{1}{2} n\pi \frac{m}{n} b_m &= \frac{1}{2} n\pi C_1^m a_m \end{aligned} \quad (4.26)$$

ensure matching of both vertical and horizontal velocities defined by (4.22) and (4.23) at the vertical locations  $-h + r < \tilde{z} < -\delta/2$  (figure 13b). The amplitudes  $A_w^m$  and  $A_u^m$  of the vertical and horizontal velocity components for the  $m$ th mode are

$$\begin{aligned} A_w^m &= |C_3^m a_m| = \left| \frac{4m^2 (n\gamma \cos(\gamma d/2) + m \sin(\gamma d/2))}{\pi n^4 [(m^2/n^2 - \gamma^2) \sin(\gamma\delta) + 2\gamma m/n \cos(\gamma\delta)]} Q_2^m \exp\left(\frac{m\delta}{n}\right) \right|, \\ A_u^m &= |C_4^m a_m| = \left| \frac{4m^2 (m \cos(\gamma d/2) - \gamma \sin(\gamma d/2))}{\pi n^4 [(m^2/n^2 - \gamma^2) \sin(\gamma\delta) + 2\gamma m/n \cos(\gamma\delta)]} Q_2^m \exp\left(\frac{m\delta}{n}\right) \right|. \end{aligned} \quad (4.27)$$

The singularity leading to infinite velocity amplitude appears if (4.20a) or (4.20b) is satisfied. The amplitude of the vertical velocity at the antinode  $(\tilde{x}, \tilde{z}) = (\pi, 0)$  is dominated by the contribution of the  $n$ th mode, provided  $\alpha$  is close to  $\alpha_*$ :

$$A_w = A_w^n = \left| \frac{4(\gamma \cos(\gamma\delta/2) + \sin(\gamma\delta/2))}{\pi n [(1 - \gamma^2) \sin(\gamma\delta) + 2\gamma \cos(\gamma\delta)]} Q_2^n \exp\left(\frac{\delta}{2}\right) \right|. \quad (4.28)$$

The amplitude is inversely proportional to the detuning  $\beta$ :

$$\beta = \alpha - \alpha_*, \quad (4.29)$$

since  $(A_w)^{-1} = 0$  for  $\beta = 0$ . The Taylor expansion in the vicinity of  $\beta = 0$  yields

$$(A_w)^{-1} = \left| \frac{d(A_w^n)^{-1}(\gamma_*)}{d\gamma} \frac{d\gamma}{d\beta} \right| |\beta|, \quad \gamma_* = \gamma_n^1 = \sqrt{\frac{2}{\alpha_*^2 \delta} - 1}. \quad (4.30)$$

The slope of the linear dependence of the inverse amplitude on the detuning depends only on  $\delta$ , since  $\gamma_*$  and the corresponding eigenfrequency  $\alpha_*$  are given by (4.20a) and (4.19), respectively. Calculations show that this slope varies within 5 % for  $0 < \delta < 1$ . The limit for  $\delta \rightarrow 0$  is

$$(A_w)^{-1} = \frac{n\pi}{Q_2^n} |\beta|. \quad (4.31)$$

#### 4.4. Effect of dissipation

Accounting for the dissipation due to the friction at the front and back walls of the basin within the Stokes layer model can be performed similarly, since the corresponding generalisation of the Taylor–Goldstein equation (4.14) retains a similar form (see Appendix A for details):

$$\begin{aligned} W_m'' + \left( \frac{2}{\alpha^2(1+s)} \tilde{N}^2 - 1 \right) \frac{m^2}{n^2} W_m &= 0, \\ s = \sqrt{2}(1+i) \sqrt{\frac{\mu}{\rho_0 B^2}} &\sim 10^{-2}, \end{aligned} \quad (4.32)$$

where  $\mu$  is the dynamic viscosity. The form (4.14) is obtained from (4.32) defining the effective detuning as

$$\beta' = \beta + \frac{s\alpha_*}{2}. \quad (4.33)$$

Equation (4.31) shows that the maximum amplitude is inversely proportional to  $|s|$  and corresponds to  $\beta = -\alpha_* \text{Re}(s)/2 < 0$ . The Stokes layer dissipation model does not account for viscous interaction between the wavemaker and the liquid; thus, for comparison with the experiments,  $s$  can be treated as a free parameter of the order of  $10^{-2}$ .

The dissipation in bulk is more significant for the shorter waves. The solution in the upper liquid is governed by the fourth-order equation (see [Appendix A](#) for details)

$$W_m^{IV} - 2\frac{m^2}{n^2}W_m'' + \frac{m^4}{n^4}W_m = -iRe \left[ (1+s)W_m'' + \left( \frac{2}{\alpha^2}\tilde{N}^2 - 1 - s \right) \frac{m^2}{n^2}W_m \right],$$

$$Re = -\frac{\rho_0\omega}{k_n^2\mu} \sim 10^4, \quad (4.34)$$

with boundary conditions

$$W_m \rightarrow 0, \quad \tilde{z} \rightarrow \infty,$$

$$W_m''(-\delta/2) - \frac{m^2}{n^2}W_m(-\delta/2) = 0,$$

$$W_m'''(-\delta/2) - \frac{m^2}{n^2}W_m'(-\delta/2) = 0, \quad (4.35)$$

that ensure vanishing of the velocity amplitude at infinity and matching to the potential solution in the lower liquid. The solution for  $W_m$  is found numerically, then smoothly extended to the region  $\tilde{z} < -\delta/2$ . The above-described matching procedure is then applied.

Correction to the eigenfunctions  $\varphi_{2,m}$  to account for the finite wavemaker size by imposing boundary conditions (4.11) does not change the procedure significantly. The contribution of the eigenfunctions to the  $m$ th spatial mode is a sum of  $\exp(m\tilde{z}/n)$  and  $\exp(-m\tilde{z}/n)$ . Matching of the vertical velocity and its  $\tilde{z}$  derivative at any point  $\tilde{z}_c \in (-h+r, -\delta/2)$  ensures the matching of the solutions in the entire region  $-h+r < \tilde{z} < -\delta/2$ . The coefficients  $a_m$  and  $b_m$  in the decompositions (4.23) and (4.10) are found from the system of equations

$$\frac{1}{2}n\pi a_l W_l(\tilde{z}_c) - \int_{-\pi}^{(n-1)\pi} \left[ \sum_{m=1}^{\infty} b_m \frac{\partial \varphi_{2,m}(\tilde{x}, \tilde{z}_c)}{\partial \tilde{z}} + \frac{\partial \varphi_0(\tilde{x}, \tilde{z}_c)}{\partial \tilde{z}} \right] \cos\left(\frac{l}{n}(\tilde{x} + \pi)\right) d\tilde{x} = 0,$$

$$\frac{1}{2}n\pi a_l W_l'(\tilde{z}_c) - \int_{-\pi}^{(n-1)\pi} \left[ \sum_{m=1}^{\infty} b_m \frac{\partial^2 \varphi_{2,m}(\tilde{x}, \tilde{z}_c)}{\partial \tilde{z}^2} + \frac{\partial^2 \varphi_0(\tilde{x}, \tilde{z}_c)}{\partial \tilde{z}^2} \right] \cos\left(\frac{l}{n}(\tilde{x} + \pi)\right) d\tilde{x} = 0,$$

$$l = 1 \dots \infty. \quad (4.36)$$

For arbitrary density gradient distribution  $\tilde{N}(\tilde{z})$ , a boundary  $\tilde{z}_*$  is selected so that  $\tilde{N}(\tilde{z}) \ll 1$  for  $\tilde{z} < \tilde{z}_*$ . The boundary conditions (4.35) are set at  $\tilde{z}_*$ , and the matching conditions (4.36) are also applied there. The analytical inviscid results for the piecewise-constant  $\tilde{N}(\tilde{z})$  as well as the numerical computations based on the present model confirm that the results practically do not depend on the particular choice of  $\tilde{z}_*$ .

#### 4.5. Numerical results

The numerical calculations are performed for the measured Gaussian buoyancy frequency distribution (2.5); the vertical velocity distribution is given by (4.23) and the corresponding horizontal velocity is

$$u = \frac{1}{2} \left[ \sum_{m=1}^{\infty} \frac{n}{m} a_m W_m(\tilde{z})' \sin\left(\frac{m}{n}(\tilde{x} + \pi)\right) + \text{c.c.} \right]. \quad (4.37)$$

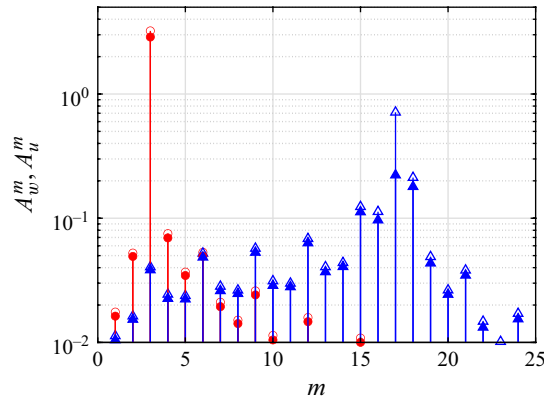


Figure 14. Wavenumber spectra of vertical (red) and horizontal (blue) velocity components at  $z = 0$  at an effective resonance  $\alpha = 0.94$  for  $\delta = 0.24$ ; open symbols account for dissipation in Stokes layers only, filled symbols for bulk dissipation as well.

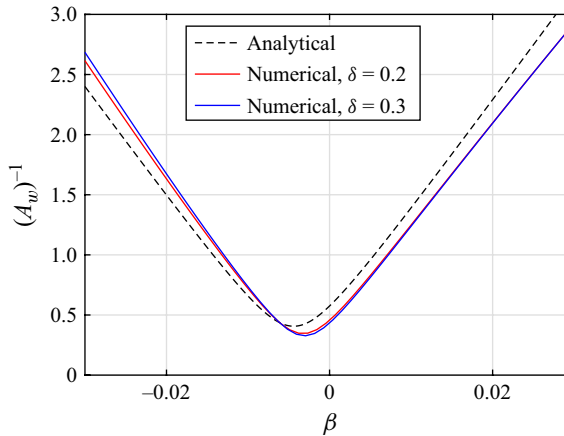


Figure 15. Inverse amplitude of the vertical velocity as a function of the detuning.

Figure 14 shows an example of wavenumber amplitude spectra of vertical and horizontal velocities at  $\tilde{z} = 0$  accounting for the Stokes layer and both dissipation mechanisms discussed above. The wavenumber domains with dominant contributions to the vertical and the horizontal velocity components are clearly separated,  $m = 3$  and  $m \approx 17$ , respectively, close to the wavenumbers that satisfy the dispersion relation for the symmetric and anti-symmetric eigenfunctions. The effect of the bulk dissipation on the longer-mode amplitude is largely insignificant but is observed for the shorter modes. The dependence of the resonant amplitude modes on the detuning  $\beta$  agrees with the simplified model predictions (4.31) as confirmed by the comparison of the inverse amplitude values in figure 15.

The amplitudes of the antisymmetric short modes with relatively large values of  $m$  depend on the detuning  $\beta$  in a complex way. Three modes with largest amplitudes are shown in figure 16 for two different pycnocline dimensionless thicknesses  $\delta$ ; the range of the corresponding values of  $m$  shifts to the left as  $\delta$  increases, in agreement with figure 12. For all modes in figure 16, a local amplitude maximum is located at  $\beta \approx -\text{Re}(s)/2$ . The appearance of this maximum can be attributed to the fact that due to the presence of the finite-size wavemaker eigenfunctions  $\varphi_{2,m}$  have complicated wavenumber spectra at any

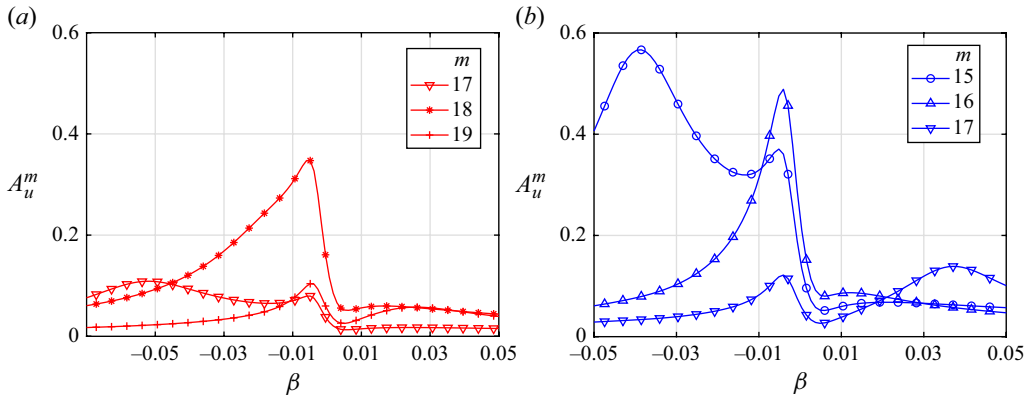


Figure 16. Amplitudes of horizontal velocity of dominant antisymmetric modes for (a)  $\delta = 0.2$  and (b)  $\delta = 0.3$ .

fixed vertical location  $\tilde{z}$ . The response curve for the mode with the eigenfrequency closest to the resonance eigenfrequency has a single maximum. The neighbouring modes exhibit additional resonances; the corresponding frequencies increase monotonically with  $m$ . The amplitudes of these resonances are proportional to the forcing at the corresponding modes (figure 11b), and thus the maximum amplitudes of the modes with  $m = n, 2n, \dots$  are larger than those of the neighbouring ones.

Experimental validation of the predicted properties of the wavefield structure within a finite-thickness pycnocline cannot be obtained using the shadowgraph technique described in § 3. Therefore, additional series of measurements in which the PIV technique was applied have been performed.

## 5. Particle image velocimetry experiments

### 5.1. Procedure

The PIV set-up consists of a continuous 532 nm laser (1.5 W) with light sheet generation optics (see figure 1). To minimise the optical distortions caused by density gradient in the imaged area (Dalziel *et al.* 2000), the laser sheet is placed at a distance of 10 mm, sufficiently close to the front wall out of the Stokes layer. A 3.2 MPixel USB 3.1 camera (FLIR Blackfly) operating at 5 Hz recorded the flow field. Silver-coated hollow 10  $\mu\text{m}$  glass spheres served as the tracers. LaVision Davis software was used to compute the two-dimensional instantaneous velocity field; the interrogation cell size was  $48 \times 48$  pixels with 50 % overlap, corresponding to a spatial resolution of  $0.13 \text{ mm px}^{-1}$ . The temporal resolution defined by the camera frame rate corresponds to approximately 30 frames per wave period. The imaged area spans almost half a wavelength of the third standing-wave mode and is centred at its antinode. Supplementary movie 2 shows the maps of the vertical and horizontal velocity components normalised by the wavemaker velocity amplitude.

The experiments were carried out for amplitude of the wavemaker displacement  $F = 7.5 \text{ mm}$ ,  $n = 3$ , forcing frequency corresponding to  $0.905 \leq \alpha \leq 0.946$  and  $0.18 < \delta < 0.43$ . As in the shadowgraph experiments, the mean position of the wavemaker centre was 350 mm above the bottom of the tank. Before each series of experiments, the basin was refilled as described in § 2. To decouple the effect of frequency detuning and the pycnocline thickness  $d$ , in each series of PIV experiments, the forcing frequency was kept constant while in the course of the successive runs  $d$  gradually increased. At every  $\alpha$ , the experimental series consisted of 12–20 runs. The first run started from rest, then the wavemaker motion was initiated and lasted for 300 cycles; after that, the wavemaker

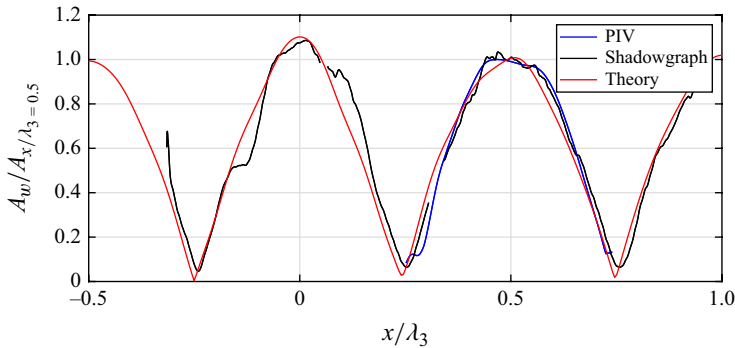


Figure 17. Vertical velocity amplitude along the upper pycnocline boundary  $\tilde{z} = \delta$ , normalised by the corresponding value at  $x/\lambda_3 = 0.5$  for PIV measurement, shadowgraph measurement and theory at the corresponding effective resonant conditions ( $\alpha = 0.917$ ,  $\delta = 0.32$ ;  $\alpha = 0.931$ ,  $\delta = 0.22$ ;  $\alpha = 0.925$ ,  $\delta = 0.306$ , respectively).

stopped and paused for 10 min during which the waves fully decayed allowing the initiation of the next run. The density profile was measured by a PCP before the initiation of the series and between the runs at the end of the wavemaker pause.

The consistency between PIV and shadowgraph measurements and the theoretical model is examined by the comparison of normalised vertical velocity amplitude distribution along the horizontal line  $\tilde{z} = \delta$  in figure 17. The velocity amplitudes are normalised by the corresponding values at the third-mode antinode  $x/\lambda_3 = 0.5$ ; the curves are plotted at the corresponding effective resonant conditions. A good agreement is observed, although the coverage of two experimental datasets is different.

Figure 18 presents a summary of the experimental conditions in the present experiments, along with the theoretically obtained dispersion relation  $\alpha(k_3 d)$  and the theoretical estimates of the effect of the finite wavemaker size and the dissipation. Each set of horizontal circles at a constant forcing frequency represents a single series of experimental runs as specified above. It demonstrates the natural widening of the pycnocline during each series. The colour of the circles corresponds to the amplitude of the vertical velocity oscillations at the antinode ( $x/\lambda_3 = 0.5$ ) after a quasi-steady state is attained for the given operational parameters.

## 5.2. Particle image velocimetry data analysis

### 5.2.1. Response curves

Numerous experiments carried out under diverse experimental conditions allow decoupling of the effect on the wavefield of the pycnocline thickness and of the forcing frequency. The horizontal and vertical sections of the diagram in figure 18 yield the experimentally measured variation of the system response to the forcing as a function of the dimensionless pycnocline thickness  $\delta$  at fixed frequency, and of the dimensionless forcing frequency  $\alpha$  at fixed pycnocline thickness. Typical examples of the resulting curves are plotted in figure 19. The system response is represented by the amplitude of the vertical velocity component at the third-mode antinode normalised by the amplitude of the wavemaker velocity  $A_w(x/\lambda_3 = 0.5, z = 0)$ . The amplitude variation with the pycnocline thickness for a fixed frequency does not change notably with  $\alpha$ . The effective resonance frequency decreases with an increase in  $\delta$ , while the maximum amplitude exhibits only a weak change. The normalised amplitude at the effective resonance is significantly smaller than those measured for the similarly excited surface

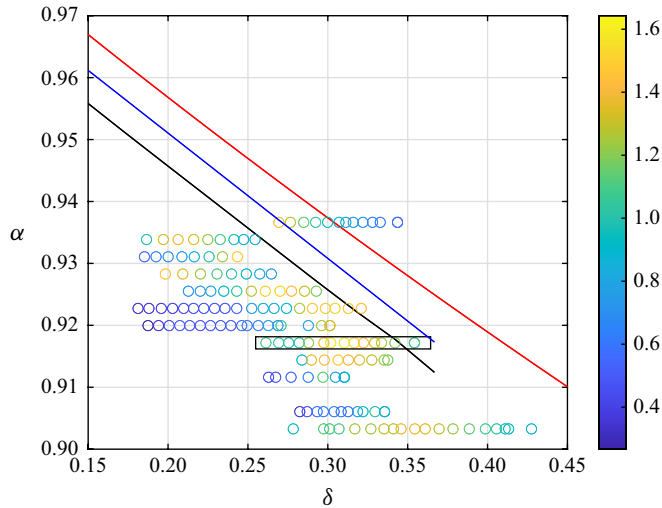


Figure 18. Diagram of the experimental conditions. The symbols represent the experimental results, with the colour showing the vertical velocity amplitude at the antinode ( $x/\lambda_3 = 0.5$ ) normalised by the wavemaker velocity amplitude. The lines correspond to the eigenfrequency of the rectangular basin (red), the resonant frequency for the basin with the immersed wavemaker (blue) and the effective resonant frequency accounting for dissipation (black).

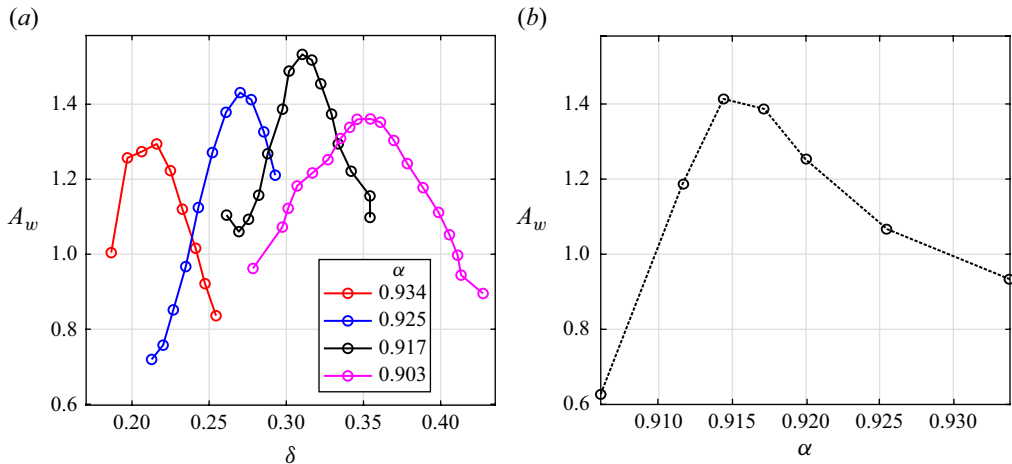


Figure 19. The amplitude of the vertical velocity oscillations at the antinode ( $x/\lambda_3 = 0.5$ ) of the third-mode standing wave from PIV measurements: (a) as function of the pycnocline thickness for different forcing frequencies; (b) as function of frequency for constant pycnocline thickness  $\delta = 0.305$ .

waves (Mogilevskiy *et al.* 2024) that represent a limit case  $\delta \rightarrow 0$  with negligible dissipation in the pycnocline.

The viscous model yields similar results (figure 20). The downshift of the effective resonance frequency is somewhat underestimated, while the normalised amplitude at the effective resonance is nearly twice larger than in the experiments. As in the experiments (figure 19a), the maximum of the normalised amplitude practically does not vary with  $\alpha$ .

Measurements of the vertical velocity amplitude at the antinode are summarised in figure 21 as a function of the detuning  $\beta = \alpha - \alpha_*(\delta)$ . Note that the figure contains about 160 data points, each representing a separate experimental run more than 10 minutes

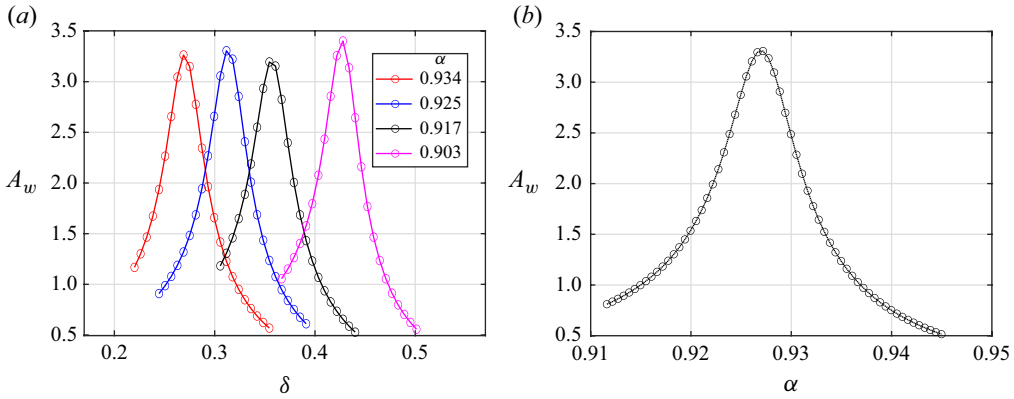


Figure 20. The results of the theoretical model accounting for the full dissipation for parameters as in figure 19.

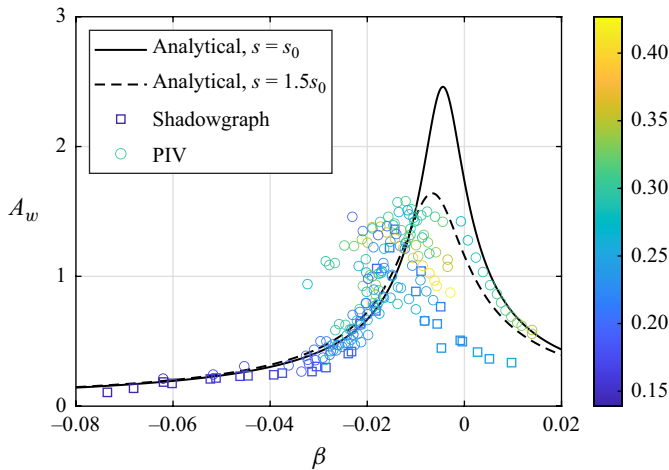


Figure 21. Normalised amplitude of the vertical velocity at the antinode as a function of the detuning. The colour of the experimental points corresponds to the pycnocline thickness  $\delta$ ; the value of dissipation coefficient  $s_0$  corresponds to experiments.

long. Both shadowgraph- and PIV-derived results collapse onto close vicinity of a single curve. The measured data agree well with the linear theory (4.31) far below the resonance. The discrepancy of the measured maximum amplitude and of the corresponding detuning cannot be attributed solely to the effect of dissipation; thus, the effect of nonlinearity may also be significant. Indeed, selection of the value of the dissipation coefficient  $s$  to fit the maximum amplitude within the linear computational model does not cause a notable shift in the detuning at the effective resonance. To resolve this discrepancy by accounting for nonlinearity, advantage can be taken of close similarity between nonlinear resonant free-surface waves (Mogilevskiy *et al.* 2024) and those at the interface between the two liquids. Adjustments of their model to the present problem result in the estimation of the downshift of the effective resonance frequency  $(k_n Fr^2 / (h - \delta))^{2/3} \approx 0.02$ , in good agreement with experiments.

### 5.2.2. Symmetric and antisymmetric modes in the velocity field at the forcing frequency

The series of experimental runs carried out at a constant forcing frequency  $\alpha = 0.917$  (marked by a rectangular box in figure 18) is now considered. To analyse the wavefield at

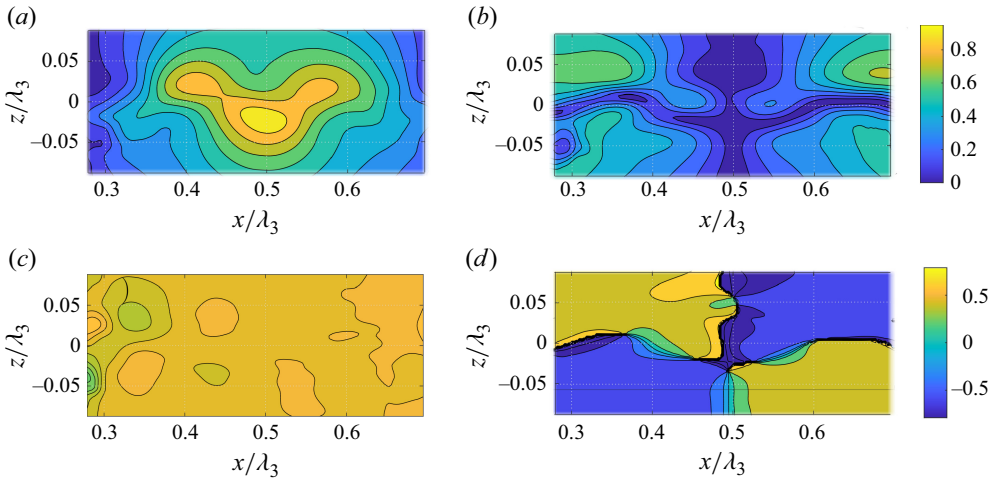


Figure 22. Spatial distributions of the velocity components for  $\delta = 0.282$  band-pass-filtered at the forcing frequency  $\alpha = 0.917$ . (a,b) Amplitudes  $A_{w,u}$ ; (c,d) phase shift  $\theta_{w,u}$  in time (in  $\pi$  units) relative to the wavemaker displacement; (a,c) vertical velocity component  $w$ ; (b,d) horizontal velocity component  $u$ . Supplementary movie 3 shows the variation of maps of both band-pass-filtered velocity components.

the forcing frequency, the PIV signal was band-pass-filtered at each spatial location  $(x, z)$  independently, resulting in periodic in time functions:

$$u^1(t, x, z) = A_u(x, z) \cos(\omega t + \theta_u), \quad w^1(t, x, z) = A_w(x, z) \cos(\omega t + \theta_w). \quad (5.1)$$

The contour maps of the spatial distribution of the dimensionless amplitudes and phases of the vertical  $w$  and the horizontal  $u$  velocity components are presented in figure 22. The distributions are dominated by the mode with  $m = 3$ , although the short-scale features are also present.

The dispersion relation (figure 12) indeed allows coexistence at the forcing frequency of the dominant symmetric mode with  $m = 3$  and of the higher antisymmetric modes with  $m$  ranging from 15 to 17 (depending on the dimensionless pycnocline thickness  $\delta$ ). To examine this conjecture, the third spatial mode is first identified in the recorded velocity distributions, and the assumption of the dominance of this standing-wave mode in the wavefield is verified. To this end, for each frame corresponding to instant  $t$  and each  $z$  independently, the distributions of both velocity components normalised by the wavemaker velocity amplitude  $\omega F$  were fitted to

$$u^{fit}(t, x, z) = u_3(t, z) \cos(k_3 x + \gamma_u(t, z)), \quad w^{fit}(t, x, z) = w_3(t, z) \cos(k_3 x + \gamma_w(t, z)), \quad (5.2)$$

defining functions  $u^{fit}(t, x, z)$  and  $w^{fit}(t, x, z)$  that are periodic in time with period  $T_3$  and in the horizontal direction with the period  $\lambda_3$ ;  $u_3(t, z)$ ,  $w_3(t, z)$ ,  $\gamma_u(t, z)$  and  $\gamma_w(t, z)$  are the fitting parameters. For each location  $(x, z)$ , the time-dependent periodic functions  $u^{fit}$  and  $w^{fit}$  have amplitudes  $A_{u,w}^{fit}(x, z)$  and phase shift  $\theta_{u,w}^{fit}(x, z)$  relative to the wavemaker displacement plotted in figure 23. The patterns of the phase maps correspond to the third-mode standing wave with a practically constant  $\theta_w^{fit}(x, z)$ . The values of  $\theta_u^{fit}(x, z)$  change sharply by  $\pi$  in the vicinity of the corresponding nodes.

The profiles of the normalised vertical velocity component amplitude  $A_w(x, z)$  at the antinode  $x/\lambda_3 = 0.5$  of the band-pass-filtered record (figure 24a) are compared with

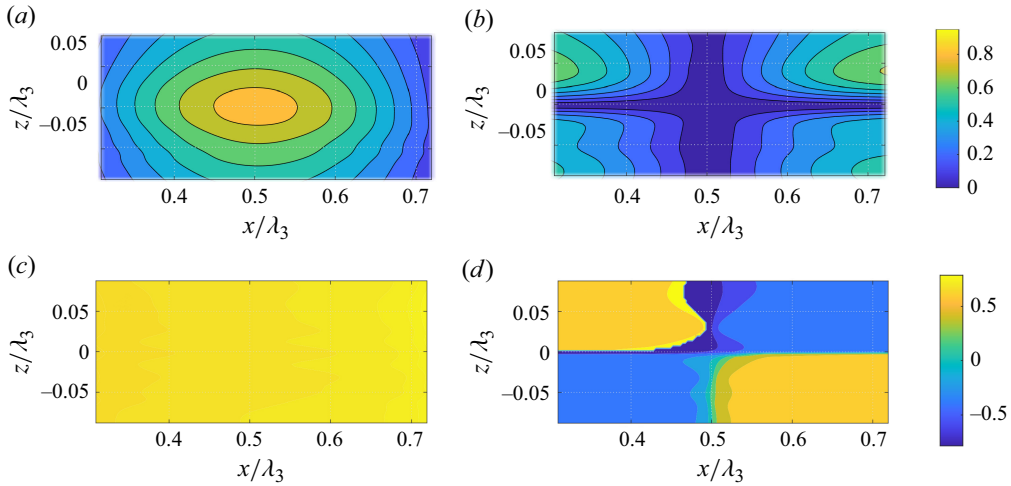


Figure 23. As in figure 22 for the fitted velocity amplitudes  $A_{u,w}^{fit}$  and phases  $\theta_{u,w}^{fit}$ . Supplementary movie 4 shows the temporal variation of maps of both fitted velocity components.

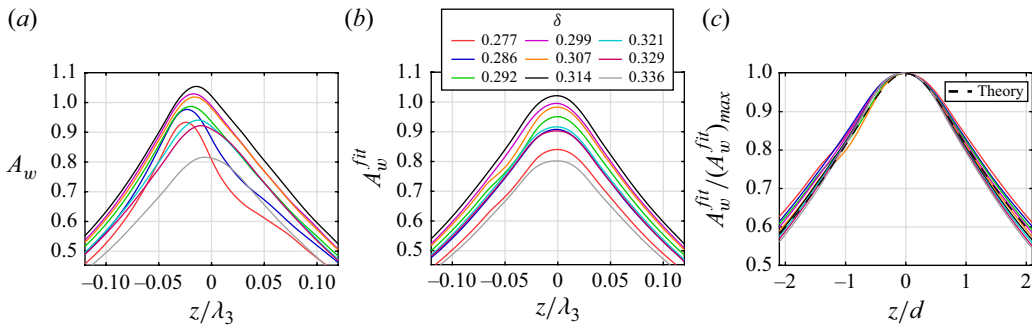


Figure 24. (a) Profiles of the vertical velocity component amplitude. (b) The fitted amplitude of the third-mode wave for different pycnocline thickness  $\delta$ . (c) The fitted distributions normalised by their maxima are compared with theoretical eigenfunction for  $m = 3$ ,  $\delta = 0.305$  and  $\alpha = 0.917$  (the black bold dashed line).

the corresponding distributions of the normalised fitted amplitudes  $A_w^{fit}$  (figure 24b) at multiple experimental runs with different values of the pycnocline thickness  $\delta$ . The shapes of the velocity amplitude profiles  $A_w(z)$  differ notably from those of the fitted distributions. The profiles obtained for different experimental conditions  $A_w^{fit}$  appear to be symmetric around  $z = 0$ ; when normalised by their maxima, they nearly collapse, with shapes that agree well with the theoretical eigenfunction of the third mode (figure 24c).

The contribution to the wavefield of the antisymmetric modes at the wavemaker forcing frequency is evaluated by computing at each instant the residual defined as

$$u^{res}(t, x, z) = u^1 - u^{fit}, \quad w^{res}(t, x, z) = w^1 - w^{fit}. \quad (5.3)$$

The maps of amplitudes  $A_{w,u}^{res}$  of the vertical and horizontal velocity components  $w^{res}$  and  $u^{res}$  presented in figure 25(a,b) exhibit a spatially quasi-periodic horizontal structure, with mean wavelength corresponding to  $m$  about 16, in agreement with the dispersion relation (figure 12). Note that the amplitudes  $A_w^{res}$  of the residual of the vertical velocity component  $w^{res}$  practically vanish along the centreline of the pycnocline  $z = 0$ , where the maxima of the horizontal velocity amplitudes  $A_u^{res}$  are located. The corresponding phase

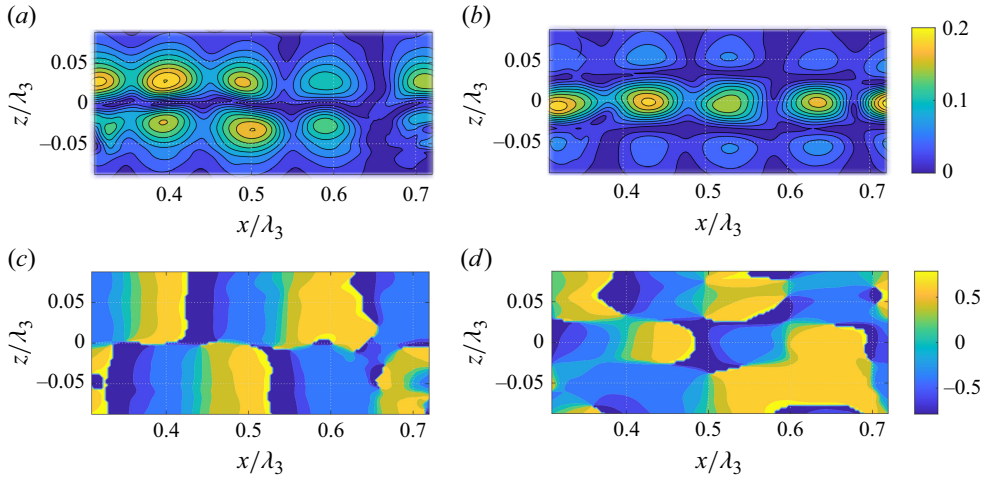


Figure 25. As in [figure 22](#) for the residual velocity amplitudes  $A_{u,w}^{res}$  and phases  $\theta_{u,w}^{res}$ . Supplementary movie 5 shows the temporal variation of maps of both residual velocity components.

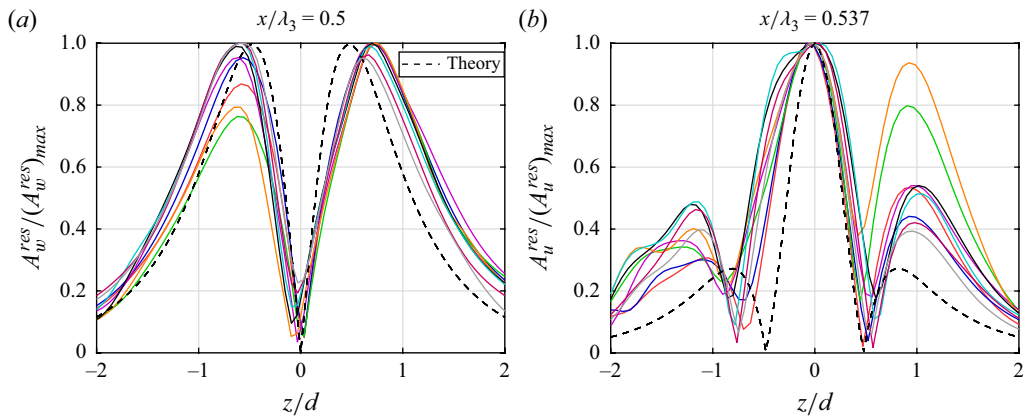


Figure 26. Profiles of normalised amplitudes of (a) residual vertical velocity component at  $x/\lambda_3 = 0.5$  and (b) residual horizontal velocity component at  $x/\lambda_3 = 0.537$  for different pycnocline thickness. In (a,b), theoretical curves correspond to  $m = 16$  and  $\delta = 0.306$ ; colours as in [figure 24](#).

maps are presented in [figure 25\(c\)](#) and [25\(d\)](#), respectively. The phase shift of  $\pi$  between the two maxima of the residual of the vertical velocity amplitude confirms that the wave is antisymmetric around  $z = 0$ .

The estimated vertical profiles of the normalised amplitudes of the residuals of the vertical and horizontal velocity components are now compared with the theoretical eigenmodes for  $m = 16$  for different values of the pycnocline thickness  $\delta$ . The profiles are plotted for the antinode locations of the corresponding velocity components:  $x/\lambda_3 = 0.5$  and  $x/\lambda_3 = 0.537$ , respectively ([figure 26a,b](#)). The theoretical curve computed for  $m = 16$  and  $k_3 d = 0.306$  is compared with the experimental profiles normalised by their maxima and agree reasonably well.

The adopted data processing procedure allows decomposition of the complex wavefield into coexisting different symmetric and antisymmetric spatial modes at the single forcing frequency. The wave is dominated by a single symmetric eigenmode, over which a weaker

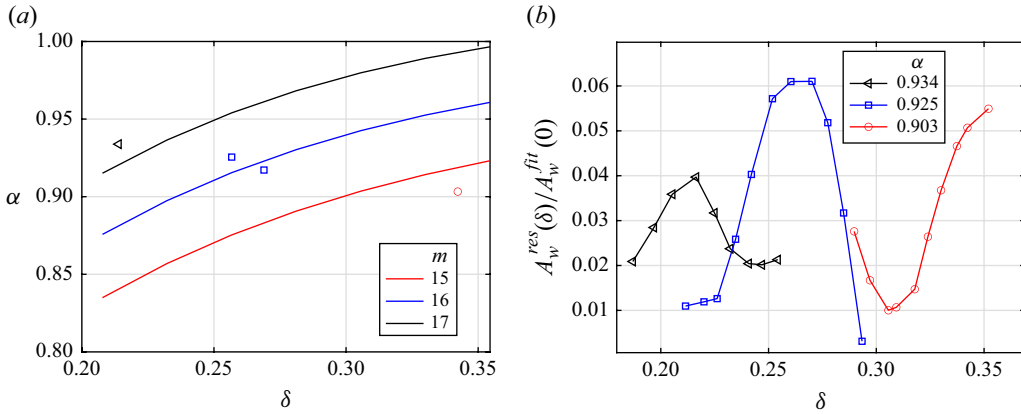


Figure 27. (a) Normalised frequency  $\alpha$  as a function of  $\delta$  for antisymmetric modes with  $15 \leq m \leq 17$ . The markers correspond to the experimentally observed modes. (b) The response curves of the antisymmetric mode as a function of the pycnocline thickness  $\delta$  for different values of  $\alpha$ .

and shorter antisymmetric wave is superposed. The effective wavemode number  $m$  of the antisymmetric mode was obtained from the mean distance between the consecutive maxima of the residual vertical velocity amplitude (figure 25a). The measured values agree with the theoretically predicted values based on the dispersion relation for the range of  $\alpha$  and  $\delta$  adopted in the experiments (figures 12a and 27a). The variation of the measured normalised amplitudes of the antisymmetric mode with the pycnocline thickness  $\delta$  for different constant forcing frequencies is presented in figure 27(b).

### 5.2.3. Second frequency harmonic

The shadowgraph experiments presented in § 3 indicate that the interface has a complex structure not just in space but also in time, with the second harmonic in the frequency that cannot be neglected (figure 8). Its excitation can be attributed to nonlinear interaction of the primary wave with itself, as well as to the temporal variation of the wavemaker immersion depth relative to the pycnocline; see (4.5b) and boundary condition (4.6d) that account for the variable wavemaker position.

The PIV-derived temporal variation of the vertical velocity component measured at the third-mode antinode  $x/\lambda_3 = 0.5$  is dominated by the contributions of the two lowest-frequency harmonics  $\alpha$  and  $2\alpha$ . Figure 28 supports this statement for the forcing frequency  $\alpha = 0.917$  and different values of  $\delta$ .

The main features of the second harmonic can be predicted based on the linear dispersion relation (figure 12a). A contour map of the vertical velocity component amplitude band-pass-filtered at double the wavemaker frequency presented in figure 29(a) is characterised by a quasi-periodic wave pattern. The vertical amplitude profile has a single maximum within the pycnocline at  $z \approx 0$  which is a fingerprint of a symmetric eigenmode. The estimated mode number  $m \approx 20$  is in agreement the linear theory. The two-layer model predicts a second-harmonic wave with mode number  $m = 12$ ; accounting for the finite thickness of the pycnocline upshifts the resonant mode number considerably. For the range of  $\delta$  and  $\alpha$  in the present experiments, the slope of the dispersion curve in figure 12(a) at the vicinity of  $m$  corresponding to the second frequency harmonic is quite small. This enables coexistence in the wavefield of multiple neighbouring resonant standing modes, resulting in complex measured spatial distributions of the vertical velocity component amplitudes (figure 29b).

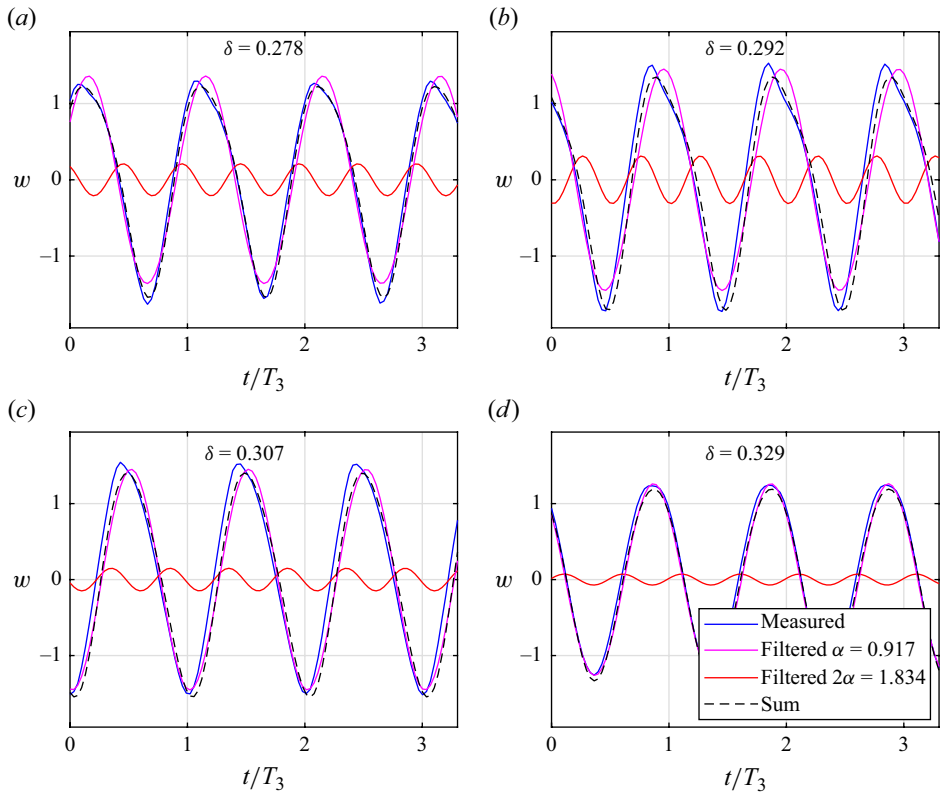


Figure 28. Decomposition of the temporal record of vertical velocity into that at forcing frequency  $\alpha$  and at double that frequency  $2\alpha$  for (a–d) different values of  $\delta$ .

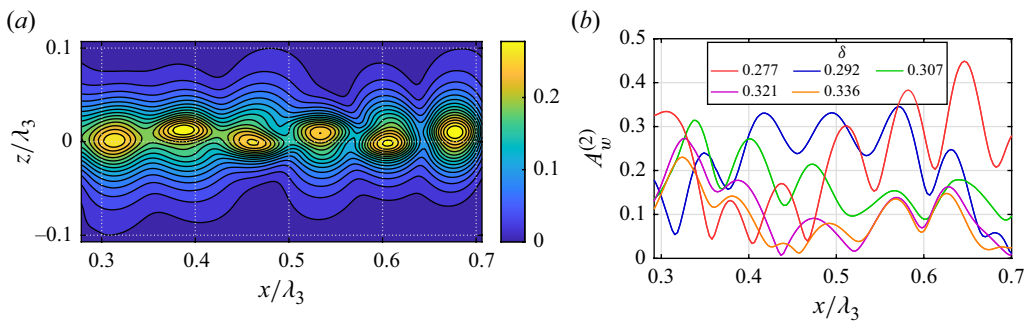


Figure 29. (a) Contour map of vertical velocity amplitude of the second harmonic  $A_w^{(2)}$  (normalised by the wavemaker velocity amplitude) for  $\delta = 0.342$  and  $\alpha = 0.903$ . (b) The spatial distribution of the normalised amplitude profiles of the second harmonic of the vertical velocity component at  $z=0$ , for different  $\delta$ . Supplementary movie 6 shows the temporal variation of the map of the band-pass-filtered vertical component.

## 6. Conclusions

This study is focused on two-dimensional internal resonant standing waves excited by a cylinder vertically oscillating in a narrow deep basin with length  $L$  in the vicinity of the basin's eigenfrequencies. The basin is filled by stable layers of salted and pure water separated by a thin pycnocline of finite thickness  $d$ . The waves in such a system differ qualitatively from those observed at the interface of two immiscible fluids

(Mogilevskiy *et al.* 2024), as well as from internal waves within a fluid with a constant density gradient (Thorpe 1968). For the pycnocline-type density distribution employed in the present study, multiple wavenumbers satisfy the dispersion relation for any given frequency (see § 4.2). Thus, a temporally monochromatic forcing excites a wavefield with a complex spatial structure that, in the steady regime, comprises multiple possible standing waves at the forcing frequency. Fourier analyses in frequency or wavenumber domains are applied to reveal the spatial and temporal structures of the waves. Wave amplitudes in frequency and in wavenumber domains, the effective resonance frequencies and the maximum possible system responses for a given wavemaker displacement amplitude are defined by dimensionless pycnocline thickness  $\delta$  and affected by dissipation. An increase in  $\delta$  downshifts the effective resonance frequency from that given by the two-layer model (equation (2.1)). Additional non-negligible spatial modes at the second temporal harmonic are excited as well.

The developed linear model yields estimates of the effect of the pycnocline thickness and of the finite size of the vertically oscillating cylindrical wavemaker on the structure of the internal wavefield resonantly excited in a narrow rectangular basin. The model accounts for the dissipation in the Stokes layers at the solid surfaces and in the bulk within the pycnocline (§ 4.4). The resulting wavefield involves superposition of two types of internal waves that correspond to symmetric and antisymmetric distributions of the vertical velocity, as followed by the analysis based on the Taylor–Goldstein equation (4.14). The model predicts how the amplitudes of both symmetric and antisymmetric modes depend on the forcing frequency. The symmetric mode amplitudes effectively depend only on the dimensionless detuning  $\beta$  (4.29), that is, the normalised deviation of the forcing frequency from the pycnocline thickness-dependent eigenfrequency (figure 15). Similarly to the case of resonant free-surface gravity waves, the finite size of the wavemaker leads to a certain downshift of eigenfrequencies. Antisymmetric modes are characterised by a different behaviour (figure 16); the wavenumber of the antisymmetric mode with the highest amplitudes changes with the detuning. The theoretical findings are compared with the results of experiments. Each experimental session consisted of a sequence of runs spanning frequencies in the vicinity of the effective resonance. Between the consecutive runs, the wavemaker was stopped for a duration sufficient for the liquid to come to rest. The measurements of the detailed vertical density profile carried out during these pauses detected broadening of the pycnocline in the course of each session.

Two independent series of experiments were carried out. First, video shadowgraphy was used in which dye was added to the salted water resulting in a clearly visible sharp interface that was captured by a video camera over nearly the whole span of the basin. The density profile measurements relate this interface to the upper boundary of the pycnocline. The temporal and the spatial variation of the recorded shape of the interface is dominated by the resonant third mode; the interface, however, also exhibits features with shorter length scales. The frequency spectra of the interface movement at any fixed lateral location  $x$  contain a major contribution at the forcing frequency, with a notable peak at its second harmonic. When all frequencies but the forcing frequency are removed by applying band-pass filtering at each lateral location separately, the wavenumber spectra of the resulting interfaces exhibit three peaks. The main peak is centred at the resonant mode; two other relatively broad peaks may be attributed to the cubic nonlinearity (mode numbers around 9) and to the presence of the antisymmetric modes with numbers around 15.

To study the internal structure of the waves within the pycnocline that cannot be revealed by shadowgraphy, the instantaneous spatial distributions of both velocity components were measured using the time-resolved PIV technique in a separate series of experiments. To resolve the wavefield within the relatively thin pycnocline, the spatial coverage of the

PIV images was reduced as compared with that in shadowgraph experiments; it was centred horizontally at the antinode of the dominant wave. In each experimental session, the forcing frequency was retained constant. Consecutive runs thus allowed the study of the variation of the system response with growing-in-time thickness of the pycnocline  $d$ . Multiple series carried out at different frequencies allowed extraction of the response curves as a function of frequency for different values of  $d$ . The measured values of the effective resonant frequencies and of the maximum wave amplitudes are somewhat lower than the predictions of the linear model even though it accounts for dissipation. The estimates based on the analogy between the internal and the free-surface two-dimensional resonant standing waves allowed attribution of the observed downshift to nonlinear effects.

A special data processing procedure has been developed to analyse the considerable body of data accumulated in the present experiments. The PIV-measured data were used to reveal the temporal and the spatial wave structure within the pycnocline. At the forcing frequency, the contributions of the long symmetric and the short antisymmetric modes are identified. The maps of the obtained amplitude distributions (figure 22) agree well with the theoretical prediction based on the Taylor–Goldstein equation. The difference between the full band-pass-filtered maps and those corresponding to the third mode only (figure 25) shows remarkable similarity to the antisymmetric eigenmodes at the corresponding eigenfrequency, with mode number  $m$  ranging from 15 to 17, depending on  $d$ . The maps of the amplitudes of the velocity component distributions obtained by band-pass filtering around double the forcing frequency (figure 29) are dominated by the symmetric mode with mode number  $m \approx 20$ , in agreement with the Taylor–Goldstein equation.

**Supplementary movies.** Supplementary movies are available at <https://doi.org/10.1017/jfm.2025.384>

**Acknowledgements.** E.M. thanks the Center for Integration in Science of the Israeli Ministry of Aliyah and Integration for support.

**Funding.** This research was supported by Pazy Foundation (grant no. 5100034339) and by Israel Science Foundation (grant no. 735/23).

**Declaration of interests.** The authors report no conflict of interest.

## Appendix A. Viscous dissipation

The non-slip conditions at the front and back walls  $y = 0$  and  $y = B = 160$  mm render the flow of viscous liquid in the system three-dimensional. Nevertheless, since the pressure remains constant across the Stokes boundary layers at the walls, the solution with two non-zero velocity components is feasible. The governing equations get additional terms due to the viscous stresses proportional to the dynamic viscosity  $\mu$ :

$$\begin{aligned}\rho_0 \frac{\partial u}{\partial t} &= -\frac{\partial p}{\partial x} + \mu \left[ \frac{\partial^2 u}{\partial x^2} + \frac{\partial^2 u}{\partial y^2} + \frac{\partial^2 u}{\partial z^2} \right], \\ \rho_0 \frac{\partial w}{\partial t} &= -\frac{\partial p}{\partial z} - \rho g + \mu \left[ \frac{\partial^2 w}{\partial x^2} + \frac{\partial^2 w}{\partial y^2} + \frac{\partial^2 w}{\partial z^2} \right], \\ \frac{\partial \rho}{\partial \tau} + w \frac{d\rho_s(z)}{dz} &= 0, \\ \frac{\partial u}{\partial x} + \frac{\partial w}{\partial z} &= 0,\end{aligned}\tag{A1}$$

where  $\rho_s(z)$  is the mean density distribution and  $\rho_0 = (\rho_1 + \rho_2)/2$ . The viscosity  $\mu$  is assumed constant. Averaging the equations over  $y \in (0, B)$  results in

$$\begin{aligned}\rho_0 \frac{\partial \bar{u}}{\partial t} &= -\frac{\partial p}{\partial x} + \mu \left[ \frac{\partial^2 \bar{u}}{\partial x^2} + \frac{\partial^2 \bar{u}}{\partial z^2} \right] + \frac{2}{B} \sigma_{xy}, \\ \rho_0 \frac{\partial \bar{w}}{\partial t} &= -\frac{\partial p}{\partial z} - \bar{\rho} g + \mu \left[ \frac{\partial^2 \bar{w}}{\partial x^2} + \frac{\partial^2 \bar{w}}{\partial z^2} \right] + \frac{2}{B} \sigma_{zy}, \\ \frac{\partial \bar{\rho}}{\partial t} + \bar{w} \frac{d\rho_s(z)}{dz} &= 0, \\ \frac{\partial \bar{u}}{\partial x} + \frac{\partial \bar{w}}{\partial z} &= 0,\end{aligned}\tag{A2}$$

where  $\sigma_{xy} = \mu \partial \bar{u} / \partial y$  and  $\sigma_{zy} = \mu \partial \bar{w} / \partial y$  are viscous stresses at each wall. It is assumed that the Stokes layer thickness  $\sqrt{\mu / \rho_0 \omega} \sim 1$  mm is much smaller than the basin width  $B$ , and the averaged values differ insignificantly from those in the middle of the basin; the overbars are omitted in the following. The viscous stresses are calculated for time-periodic flow from the consideration of the Stokes layer in time-periodic flow (Mei 1989). The complex amplitudes of the stresses  $\hat{\sigma}_{xy}$  and  $\hat{\sigma}_{zy}$  are related to the velocity amplitudes  $\hat{U}$  and  $\hat{W}$  as

$$\hat{\sigma}_{xy} = \frac{1+i}{\sqrt{2}} \sqrt{\rho_0 \omega \mu} U, \quad \hat{\sigma}_{zy} = \frac{1+i}{\sqrt{2}} \sqrt{\rho_0 \omega \mu} W.\tag{A3}$$

Introducing the Reynolds number

$$Re = \frac{\rho_0 \omega}{k_3^2 \mu} \sim 10^4\tag{A4}$$

and considering a single spatial mode in the representation (4.23) leads to the equation for the amplitude function of the vertical velocity at the  $m$ th mode in dimensionless form:

$$W_m^{IV} - 2 \frac{m^2}{n^2} W_m'' + \frac{m^4}{n^4} W_m = -i Re \left[ (1+s) W_m'' + \left( \frac{2}{\alpha^2} \tilde{N}^2 - 1 - s \right) \frac{m^2}{n^2} W_m \right].\tag{A5}$$

The system contains two dimensionless dissipation coefficients, the normalised Stokes layer thickness  $s$  and inverse Reynolds number  $Re^{-1}$ , that represent the dissipation due to the wall friction and shear inside the pycnocline, respectively.

Equation (A5) with boundary conditions (4.35) is solved using the finite-difference method. The block-tridiagonal system of linear algebraic equations is obtained by the transformation of the fourth-order equation (A5) to a system of two second-order equations for  $W_m$  and  $\Omega_m = W_m''$ .

## REFERENCES

- BARBER, B.C. 1993 On the dispersion relation for trapped internal waves. *J. Fluid Mech.* **252**, 31–49.  
 BENJAMIN, T.B. 1967 Internal waves of permanent form in fluids of great depth. *J. Fluid Mech.* **29** (3), 559–592.  
 BOURY, S., PEACOCK, T. & ODIER, P. 2019 Excitation and resonant enhancement of axisymmetric internal wave modes. *Phys. Rev. Fluids* **4** (3), 034802.  
 CARR, M., DAVIES, P.A. & HOEBERS, R.P. 2015 Experiments on the structure and stability of mode-2 internal solitary-like waves propagating on an offset pycnocline. *Phys. Fluids* **27** (4), 046602.

- CHENG, M.-H. & HSU, J.R.-C. 2014 Effects of varying pycnocline thickness on interfacial wave generation and propagation. *Ocean Engng* **88**, 34–45.
- DALZIEL, S.B., HUGHES, G.O. & SUTHERLAND, B.R. 2000 Whole-field density measurements by synthetic schlieren. *Exp. Fluids* **28** (4), 322–335.
- DAVIS, R.E. & ACRIVOS, A. 1967*a* Solitary internal waves in deep water. *J. Fluid Mech.* **29** (3), 593–607.
- DAVIS, R.E. & ACRIVOS, A. 1967*b* The stability of oscillatory internal waves. *J. Fluid Mech.* **30** (4), 723–736.
- DEEPWELL D. & STASTNA M. 2016 Mass transport by mode-2 internal solitary-like waves. *Phys. Fluids* **28** (5), 056606.
- DOSSMANN, Y., BOURGET, B., BROUZET, C., DAUXOIS, T., JOUBAUD, S. & ODIER, P. 2016 Mixing by internal waves quantified using combined PIV/PLIF technique. *Exp. Fluids* **57** (8), 132.
- DOSSMANN, Y., PACI, A., AUCLAIR, F. & FLOOR, JW. 2011 Simultaneous velocity and density measurements for an energy-based approach to internal waves generated over a ridge. *Exp. Fluids* **51** (4), 1013–1028.
- FALTINSEN, O.M. 1974 A nonlinear theory of sloshing in rectangular tanks. *J. Ship Res.* **18** (04), 224–241.
- FARMER, D.M., DUNGAN SMITH, J. 1980 Tidal interaction of stratified flow with a sill in knight inlet. *Deep Sea Res. A: Oceanogr Res. Papers* **27** (3–4), 239–254.
- GEVA, M., BUKAI, M., ZEMACH, E., GABAY, S., KRAKOVICH, A. & SHEMER, L. 2021 On spontaneous appearance of internal waves in an open-pool-type research reactor. *Phys. Fluids* **33** (2), 022102.
- GOLDSTEIN, S. 1931 On the stability of superposed streams of fluids of different densities. *Proc. R. Soc. Lond. A* **132A**, 524–548.
- HUSSEINI, P., VARMA, D., DAUXOIS, T., JOUBAUD, S., ODIER, P. & MATHUR, M. 2020 Experimental study on superharmonic wave generation by resonant interaction between internal wave modes. *Phys. Rev. Fluids* **5** (7), 074804.
- LAMB, H. 1932 *Hydrodynamics*. The University Press.
- LANCHON, N. & CORTET, P. 2023 Energy spectra of nonlocal internal gravity wave turbulence. *Phys. Rev. Lett.* **131** (26), 264001.
- LIGHTHILL, M.J. 1978 *Waves in Fluids*. Cambridge University Press.
- MATHUR, M. & PEACOCK, T. 2010 Internal wave interferometry. *Phys. Rev. Lett.* **104** (11), 118501.
- MEI, C.C. 1989 *The Applied Dynamics of Ocean Surface Waves*. vol. 1. World scientific.
- MILES, J.W. 1971 Internal waves generated by a horizontally moving source. *Geophys. Fluid Dyn.* **2** (1), 63–87.
- MILES, J.W. 1986 Weakly nonlinear waves in a stratified fluid: a variational formulation. *J. Fluid Mech.* **172** (–1), 499–512.
- MIROPOL'SKY, YU Z. & SHISHKINA, O.D. 2001 *Linear Theory of Propagation of Internal Waves in the Undisturbed Horizontally Homogeneous Ocean*. Springer Netherlands.
- MOGILEVSKIY, E., KALENKO, S., ZEMACH, E. & SHEMER, L. 2024 Resonant standing surface waves excited by an oscillating cylinder in a narrow rectangular cavity. *J. Fluid Mech.* **990**, A12.
- MOISEEV, N.N. 1958 On the theory of nonlinear vibrations of a liquid of finite volume. *J. Appl. Maths Mech.* **22** (5), 860–872.
- MORSE, P.M. & FESHBACH, H. 1946 *Methods of Theoretical Physics*. Technology Press.
- NEWMAN, J.N. 2018 *Marine Hydrodynamics*. The MIT press.
- PENNY, W.G. 1952 Finite periodic stationary gravity waves in a perfect liquid. *Phil. Trans. R. Soc.* **244**, 254–284.
- RODDA, C., SAVARO, S., DAVIS, G., RENEUEVE, J., AUGIER, P., SOMMERIA, J., VALRAN, T., VIBOUD, S. & MORDAN, N. 2022 Experimental observations of internal wave turbulence transition in a stratified fluid. *Phys. Rev. Fluids* **7** (9), 094802.
- SHANMUGAM, G. 2013 Modern internal waves and internal tides along oceanic pycnoclines: challenges and implications for ancient deep-marine baroclinic sands. *AAPG Bull.* **97** (5), 799–843.
- SUTHERLAND, B.R., DALZIEL, S.B., HUGHES, G.O. & LINDEN, P.F. 1999 Visualization and measurement of internal waves by ‘synthetic schlieren’. Part 1. Vertically oscillating cylinder. *J. Fluid Mech.* **390**, 93–126.
- TAYLOR, G.I. 1931 Effect of variation in density on the stability of superposed streams of fluid. *Proc. R. Soc. Lond. A* **132A**, 499–523.
- THORPE, S.A. 1968 On standing internal gravity waves of finite amplitude. *J. Fluid Mech.* **32** (3), 489–528.
- TROY, C.D. & KOSEFF, J.R. 2005 The instability and breaking of long internal waves. *J. Fluid Mech.* **543**, 107–136.
- YALIM, J., WELFERT, B.D. & LOPEZ, J.M. 2023 Superharmonic and triadic resonances in a horizontally oscillated stably stratified square cavity. *J. Fluid Mech.* **970**, A25.
- YANG, Y.J., FANG, Y.C., CHANG, M.-H., RAMP, S.R., KAO, C.-C. & TANG, T.Y. 2009 Observations of second baroclinic mode internal solitary waves on the continental slope of the northern south china sea. *J. Geophys. Res.: Oceans* **114** (C10), C10003.